



EUROPEAN
COMMISSION

Community Research



DOPAS

(Contract Number: FP7 - 323273)

Deliverable n°5.12

Assessment of watertightness and mechanical integrity of POPLU plug

Author(s)

Elisa Rautioaho, Lennart Börgesson, Mattias Åkesson, Ola Kristensson, Jouni Valli, Matti Hakala, Xavier Pintado, Kari Koskinen

Date of issue of this report: **31.8.2016**

Start date of project: 01/09/2012

Duration: 48 Months

Project co-funded by the European Commission under the Euratom Research and Training Programme on Nuclear Energy within the Seventh Framework Programme		
Dissemination Level		
PU	Public	x
PP	Restricted to other programme participants (including the Commission Services)	
RE	Restricted to a group specified by the partners of the DOPAS project	
CO	Confidential, only for partners of the DOPAS project	

Scope	Deliverable n°D5.12 (WP5)	Version:	1.0
Type/No.	Report	Total pages	2+42
		Appendixes	2
Title	Deliverable n°5.12 Assessment of watertightness and mechanical integrity of POPLU plug	Articles:	

ABSTRACT:

This report describes the computer simulations committed to assess the watertightness and mechanical integrity of the plug in reference to the POPLU experiment.

RESPONSIBLE:

Posiva Oy, Kari Koskinen

REVIEW/OTHER COMMENTS:

VTT, Erika Holt, Posiva Oy, Marja Vuorio

APPROVED FOR SUBMISSION:

Johanna Hansen, 31.8.2016

DOPAS

Deliverable n° 5.12 Version n°1.0

Dissemination level: PU

Date of issue of this report: **31.8.2016**



TABLE OF CONTENTS

1	INTRODUCTION.....	2
2	DESCRIPTION OF THE PLUG SYSTEM.....	3
2.1	Technical design of the plug concrete part.....	3
2.2	Mechanical properties of the system.....	3
2.2.1	In situ stress state.....	3
2.2.2	Rock mass parameters.....	3
2.2.3	Elastic plug parameters.....	5
2.2.4	OL-BFZ297 Parameters.....	5
3	PREDICTION OF WATERTIGHTNESS.....	10
3.1	Model description.....	10
3.1.1	Simulated cases and scenarios.....	10
3.1.2	Geometry.....	11
3.1.3	Boundary conditions.....	14
3.1.4	Initial conditions and fixed conditions.....	14
3.1.5	Material properties.....	15
3.2	Results.....	16
3.3	Comparison of main design cases.....	24
3.3.1	Effect of clay material.....	24
3.3.2	Effect of concrete beam.....	24
3.3.3	Effect of defect width.....	25
4	PREDICTION OF MECHANICAL INTEGRITY.....	26
4.1	Simulated cases and scenarios.....	26
4.2	Results.....	26
4.2.1	Displacements.....	27
4.2.2	Maximum and minimum principal stress.....	32
5	SUMMARY.....	35
5.1	Watertightness.....	35
5.2	Mechanical integrity.....	35
	REFERENCES.....	36
	APPENDIX A. ANALYTICAL SOLUTION FOR GAP INTRINSIC PERMEABILITY.....	37
	APPENDIX B. BENTONITE INTRUSION INTO POPLU SLOT.....	39

1 INTRODUCTION

The tunnel end plug as a structure belongs to the Engineered Barrier Systems (EBS). The main function of the plug is to keep swelling backfill material in its intended position and to maintain sufficient density. Its second function is to hydraulically isolate the deposition tunnel from central tunnels during the time water contents and hence total pressures differ at different sides of the plug. Whether the plug can perform the first function is most critical in conditions in which backfill has reached its maximum swelling pressure while there is no closure material emplaced at the opposing side of the plug. To make sure these functional targets are met, dimensioning of the plug involves safety factor with respect to tolerated loadings.

The plug dimensioning and the safety factors will be assessed using measurements in an *in situ* demonstration, POPLU (Posiva's tunnel end plug) experiment. POPLU is committed within the DOPAS project (Full Scale Demonstration of Plugs and Seals). The DOPAS project is jointly funded by Euratom's Seventh Framework Programme, waste management organizations and the 14 participating partners is running from September 2012–August 2016.

This report describes the computer simulations committed to assess the watertightness and mechanical integrity of the plug in reference to the POPLU experiment. In this experiment the space between the end of the tunnel and the concrete plug is planned to be pressurised with water maximum up to 10 MPa.

In hydraulic simulations, different design options for the potential seal are tested and the flow through the saturated seal at the end of the plug and the gap at the plug/rock interface is assessed. The aim of these computer simulations is to predict the leakage ratios between the different design options and leakage scenarios in fully saturated, steady-state conditions. The higher level objective of the analytical calculations and computer simulations is to assess the effectiveness and suitability of the different design options for the seal at the end of the plug. Hydraulic assessments were done by B+Tech Oy and Clay Technology Ab.

To assess the mechanical integrity of the plug and mechanical response of the host rock in the expected repository conditions, the plug's stress state and host rock's deformation is evaluated in details with computer simulations. These evaluations of the mechanical behavior of the plug are done by Pöyry Oy as well as proposals for the basis for instrumentation (instrument positions and ranges).

At the end of the project these and the hydraulic data will be compared with pointwise and other measurements available. In case the resulting comparison error is smaller than the related validation uncertainty and if the safety factor in terms of mechanical integrity in all assessments remains acceptable, the designed plug as it has been built can be judged to perform as targeted. In this connection, the plug is comprised of the concrete structure, the potential seal layer and the part of host rock in which changes in stress state are induced due to the plug pressurisation.

2 DESCRIPTION OF THE PLUG SYSTEM

2.1 Technical design of the plug concrete part

The geometries and dimensions of the plug and the potential seal are presented in Figure 2.1. The geometries follow the plug design R_M001_C by Finnmap Consulting last updated on 6.3.2013 (Mäntynen & Viita 2013).

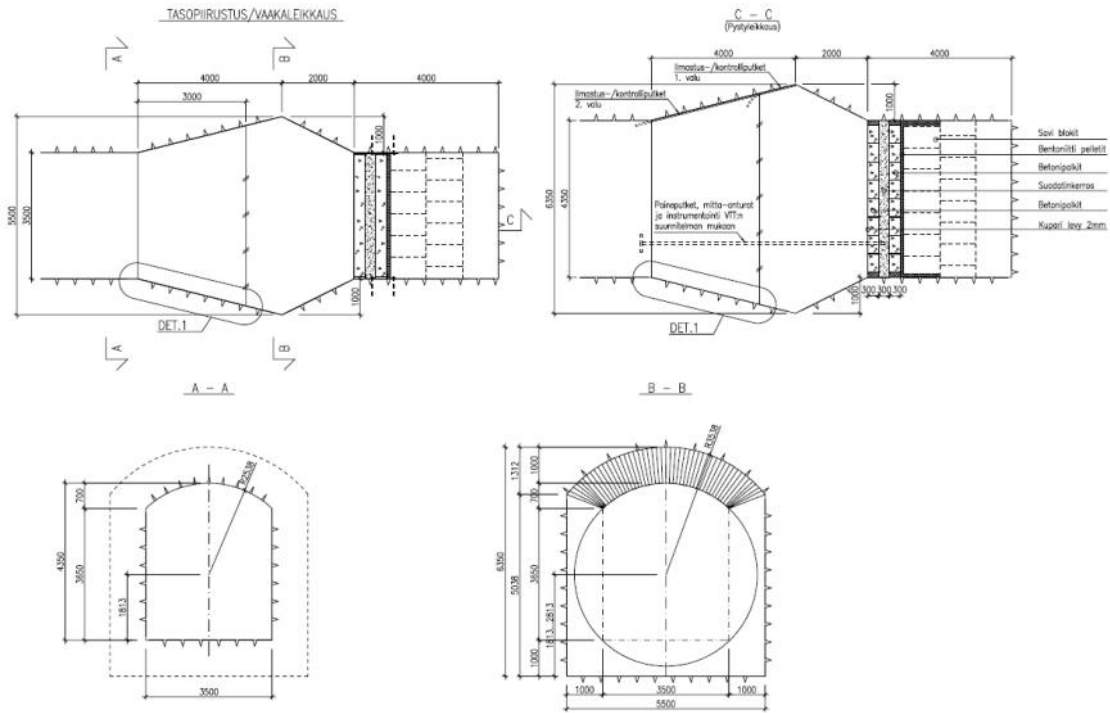


Figure 2-1. Dimensions of the plug and the seal system (drawings by Mäntynen & Viita 2013).

2.2 Mechanical properties of the system

2.2.1 In situ stress state

The in situ stress state to be used in the simulation is as defined in the Posiva Site Report (2012) with principal stress magnitudes calculated according to a depth level of -423 m (Table 2-1).

Table 2-1. In situ stress state in the simulation.

	σ_H [MPa]	σ_h [MPa]	σ_v [MPa]	Vertical depth range
Mean [MPa]	24.9	16.7	11.2	HZ20 to BFZ099
Min [MPa]	13.6	9.7	10.2	
Max [MPa]	35.7	23.7	12.3	
Orient. [°N]	112	202		

2.2.2 Rock mass parameters

Measurement results used to define the following parameters (Table 2-2) were obtained from the 2011 Posiva Site Report (Posiva 2012) and Working Report 2005-61 (Hakala et al. 2005). The uniaxial compressive strength (UCS) and tensile strength results for the foliation plane of veined

gneiss (VGN) and the VGN matrix were obtained by using their respective means and the mean UCS / T for VGN, effectively scaling the values to match previously accepted values. Results from Working Report 2011-02 were omitted as they were considered unreliable due to measurements being obtained from 4-point bend tests, a test format unrecognized by the ISRM (International Society for Rock Mechanics). Logging results of the core obtained from the pilot hole of Demo tunnel 4 were used to define the Young's Modulus of the rock mass. The foliation dip and dip direction were obtained from logging results of ONK-PH26 and ONK-PH27 (Figure 2-2).

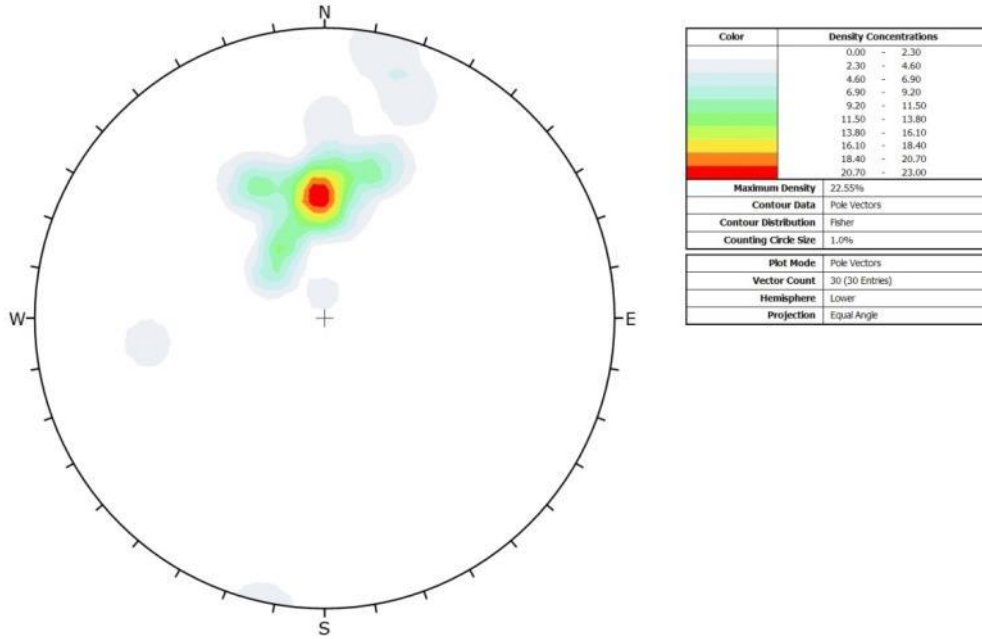


Figure 2-2. The lower hemisphere projection of the foliation measurements for VGN obtained from ONK-PH26 and ONK-PH27.

Table 2-2. Rock mass parameters.

Reference / source		VGN Matrix	VGN Foliation plane	PGR
Logging data	DIP/DD	-	45/172	-
Logging data	GSI	93	93	99
Logging data / 2012 Site report	Young's Modulus (GPa)	58	58	59
2012 Site Report	Poisson's ratio	0.25	0.25	0.29
2012 Site Report	Density (kg/m ³)	2741	2741	2635
2012 Site Report / WR 2005-61	UCS	120	96	102
2012 Site Report	Crack initiation stress σ_{ci} (MPa)	52	42	57
2012 Site Report / WR 2005-61	Initial Tensile strength (MPa)	14.1	10.1	8.9
2012 Site Report / WR 2005-61	Initial Cohesion (MPa)	19.7	15.6	19.3
2012 Site Report / WR 2005-61	Initial Friction angle (°)	16	16	22
-	Residual Tensile strength (MPa) *	0.1	0.1	0.1
1% of initial	Residual Cohesion (MPa) *	0.2	0.2	0.2
-	Residual Friction angle (°) *	53	52	53
-	Dilatation angle	20	20	20

* full mobilization of residual values requires plastic shear and tensile strain of 3e-3.

2.2.3 Elastic plug parameters

The parameters for a normal fracture representing the contact between the plug and the surrounding rock were obtained from the Posiva 2011 Site Report as values for a shotcrete / rock contact were close to parameters for a normal fracture (Table 2-3).

Table 2-3. Contact parameters.

Cohesion (MPa)	0.14
Tensile strength (MPa)	0.14
Friction (°)	28
Normal stiffness (GPa/m)	254
Shear stiffness (GPa/m)	0.22
Dilatation angle	2

The parameters for the plug were obtained from B+ Tech Oy and are defined in Table 2-4.

Table 2-4. Plug parameters.

Young's Modulus (GPa)	34
Poisson's ratio	0.2
Density (kg/m ³)	2400

The plug is assumed to be elastic in order to exhibit the maximum stresses imposed on it.

2.2.4 OL-BFZ297 Parameters

Brittle deformation zone OL-BFZ297 intersects the demonstration area of ONKALO from east to west and is observed in demonstration tunnel 1 and 2 as well as in the central tunnel. It also intersects the pilot hole for demonstration tunnel 3 as well as pilot hole ONK-PH22 (Figures 2-3, 2-4 and 2-5).

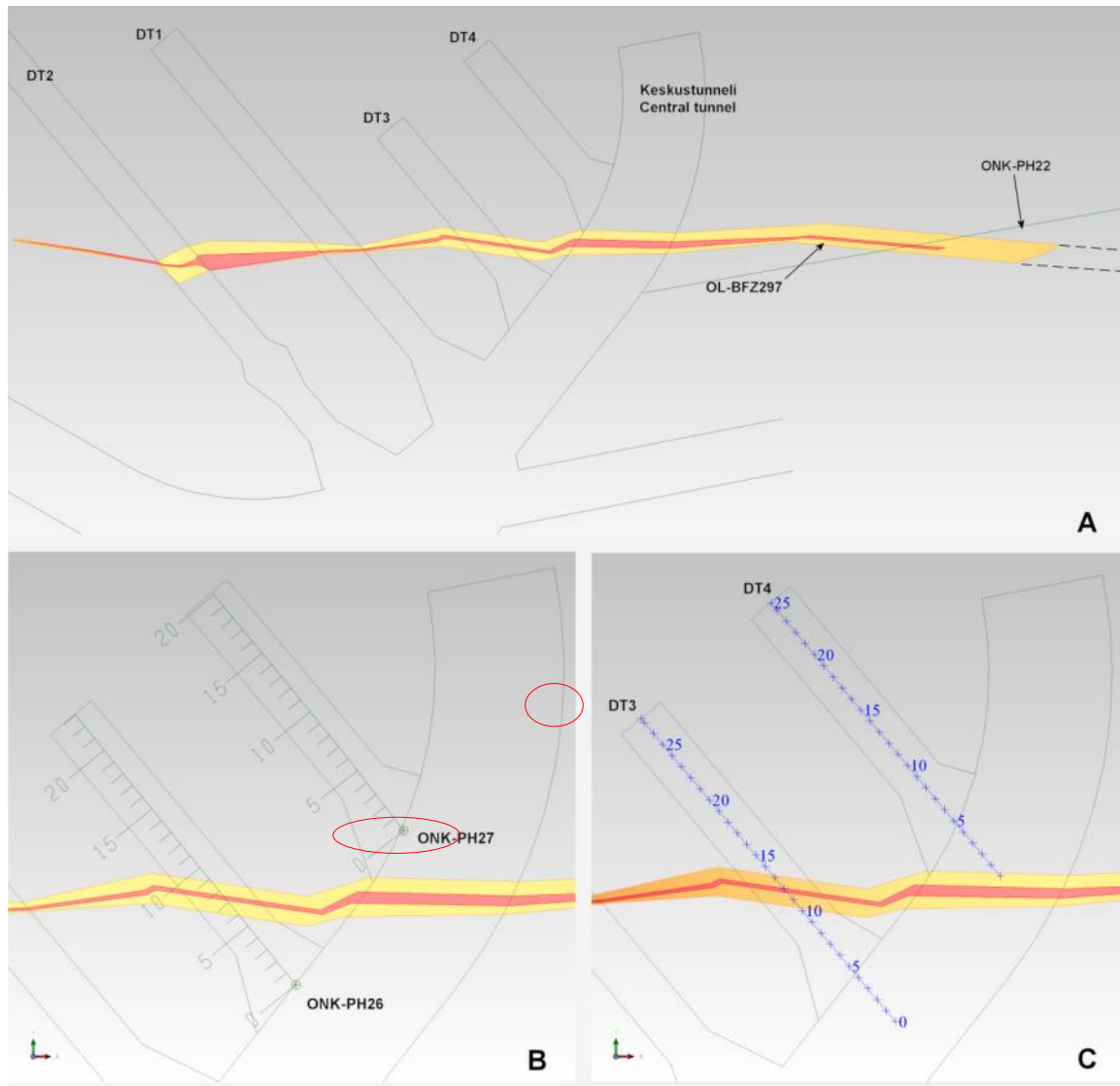


Figure 2-3. A) Plan view of OL-BFZ297 according to a depth level equivalent to the tunnel floor with the core of the zone indicated in red and its full extent of influence in yellow. B) The location of OL-BFZ297 according to logging data obtained from pilot holes ONK-PH26 and ONK-PH27, which have been cored from a height of ca. 2 m from the tunnel floor. C) The location of OL-BFZ297 with respect to the demonstration tunnel centre lines and their changes. Images B and C are both from tunnels DT3 and DT4.



Figure 2-4. A photograph of OL-BFZ297.

The dip and dip direction of OL-BFZ297 is on average $75^{\circ}/185^{\circ}$, respectively. The dip varies from roughly 60° in the west (DT2) to roughly 85° in the east (ONK-PH26, the central tunnel, ONK-PH22). The width of the core of the zone varies from a couple centimetres to ca. 30 cm and is usually composed of brecciated and crushed rock as well as clay-bearing fault gouge. Carbonates, kaolinite and chlorite are intermittently present as well as sulphides (mainly pyrite) and graphite. The core of the zone is surrounded by an influence zone, which is usually wider on the footwall side of the core and narrower, if not completely inexistent, on the hanging wall side. Slicken-side fractures, which are parallel to the trend of the zone core, and riedel- and tension fractures, which are oriented at an angle to the zone core, are often present in the influence zone. The western section of the zone exhibits large amounts of graphite and sulphides and the eastern section exhibits hydrothermal alteration (chloritisation, saussuritization, sericitization, kaolinisation). The full width of the zone including the core and influence zone is mainly 1.5–3 m.

For simulation purposes, data obtained from ONK-PH26, ONK-PH22 and the central tunnel of the demonstration area are deemed best for determining the geometrical properties of OL-BFZ297. These observations result in the following:

- Dip 84°
- Dip direction 185°
- Full width 280 cm, or:
- Core width 30 cm, influence zone 125 cm / 125 cm

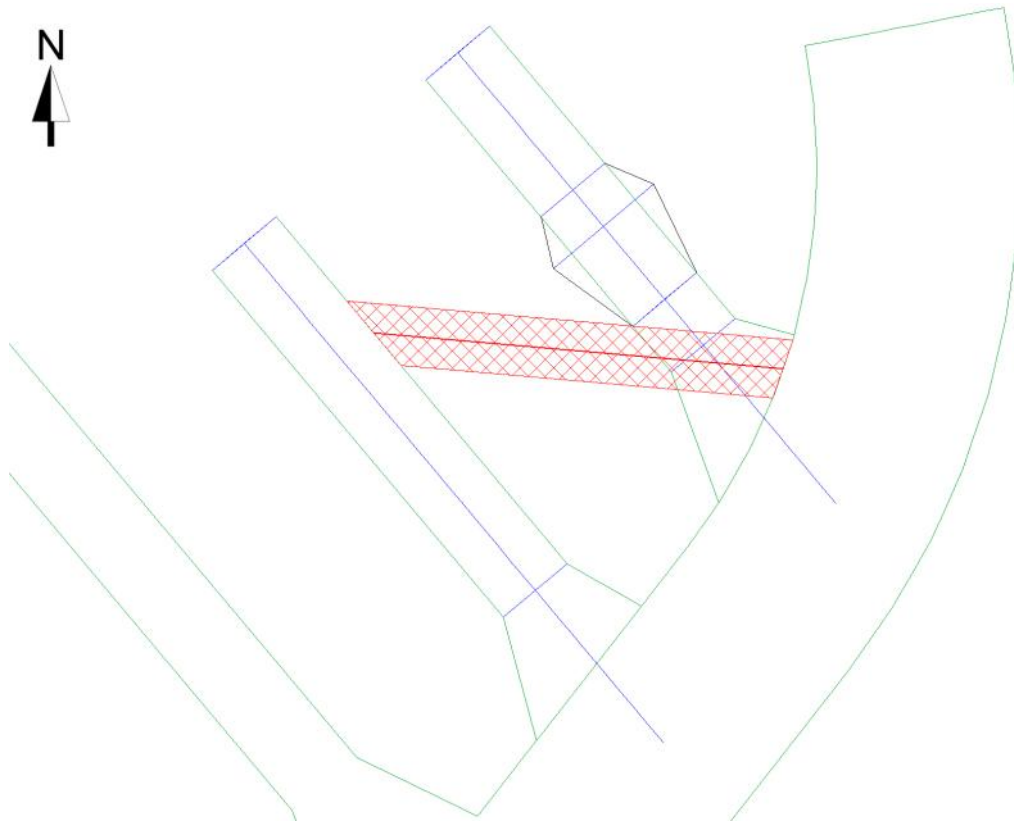


Figure 2-5. *OL-BFZ297 simulation location.*

The remaining parameters (Table 2-5) were defined using the Rock Mass Classification method described in WR 2008-67 (Hudson et al.) The GSI of the zone has hence been obtained from logging data for all of the intersections of OL-BFZ297 and the UCS has been defined according to the following method:

1. Obtain the average of the lowest Schmidt measurements representative of the zone core from OL-BFZ297, OL-BFZ100, HZ-20.
2. Obtain the average of Schmidt measurements representative of normal rock from OL-BFZ297, OL-BFZ100, HZ-20.
3. Obtain the average of Schmidt measurements representative of the influence zone from OL-BFZ297, OL-BFZ100, HZ-20.
4. Define the average ratios of BFZ vs. normal VGN and the influence zone vs. normal VGN.
5. Use these ratios to scale the UCS of VGN.
6. The normal stiffness and shear stiffness for the zone core have been defined according to the method defined in the (2009) Posiva Site Description Report, using the rock mass Young's modulus and the thickness of the core.

Table 2-5. OL-BFZ297 parameters. The common parameters are the initial values for the calculation of the core and influence zone parameters. The intact rock modulus E_i and UCS are not in the calculation. The core is modelled as a fracture, so the E_{rm} modulus is not taken into account and only the normal and shear stiffness control the stress-strain relationship.

	COMMON PARAMETERS	
DIP/DD	84/185	
Density (kg/m ³)	2741	
E _i (GPa)	60	
UCS (MPa)	108	
Poisson's ratio	0,25	
	CORE	INFLUENCE ZONE
Scale factor determined from Schmidt results	34 %	69 %
Scaled UCS	37	74
Q'	0,2	11,4
GSI	31	66
E _{rm} (GPa)	5,2	39,2
Thickness (cm)	0,3	250
Tensile strength (MPa)	0,02	0,65
Cohesion (MPa)	0,86	2,59
Friction angle (°)	28	44
Normal stiffness (GPa/m)	17,3	-
Shear stiffness (GPa/m)	6,9	-

3 PREDICTION OF WATERTIGHTNESS

A three-dimensional hydraulic numerical continuum model was created to simulate the flow through the seal and the gap in contact with the plug. The analyses were performed with the finite-element software CODE_BRIGHT (Olivella et al. 1994, 1996), which has been initially developed for modelling the non-isothermal multi-phase flow of brine, heat, liquid and gas through porous deformable saline media.

3.1 Model description

3.1.1 Simulated cases and scenarios

Three main design options were simulated:

1. Case A containing only the concrete plug and no seal material,
2. Case B containing a seal section directly behind the plug made of the current Posiva reference backfill material: Friedland clay blocks, Cebogel pellets and Minelco granules,
3. Case C containing a seal section made of high quality buffer material MX-80 bentonite blocks and MX-80 bentonite pellets, with a permeable concrete beam placed between the seal and the plug.

Additional design options were also tested to gain a better understanding of the process:

4. Case B2, i.e. case B with a permeable concrete beam placed between the seal and the plug,
5. Case C2, i.e. case C without a permeable concrete beam placed between the seal and the plug.

Two scenarios for the gap or defect at the plug/rock interface were simulated for each design option:

- I. A gap around the entire plug.
- II. A gap of 0.1 m width at the bottom of the plug.

The simulated cases are presented in Table 3-1.

Table 3-1. Case matrix.

Case	Seal materials	Concrete beam	Gap width	Gravity
A_I	-	-	Entire plug	-
A_II	-	-	0.1 m	-
Ag_I	-	-	Entire plug	X
Ag_II	-	-	0.1 m	X
B_I	Friedland-Ce-bogel-Minelco backfill	-	Entire plug	-
B_II	Friedland-Ce-bogel-Minelco backfill	-	0.1 m	-
Bg_I	Friedland-Ce-bogel-Minelco backfill	-	Entire plug	X
Bg_II	Friedland-Ce-bogel-Minelco backfill	-	0.1 m	X
B2_I	Friedland-Ce-bogel-Minelco backfill	X	Entire plug	-
B2_II	Friedland-Ce-bogel-Minelco backfill	X	0.1 m	-
C_I	MX-80	X	Entire plug	-
C_II	MX-80	X	0.1 m	-
Cg_I	MX-80	X	Entire plug	X
Cg_II	MX-80	X	0.1 m	X
C2_I	MX-80	-	Entire plug	-
C2_II	MX-80	-	0.1 m	-

3.1.2 Geometry

The geometries of the main and additional design cases in the two leakage scenarios (I and II) are presented in Figures 3-2 to 3-6. The geometries follow the plug design R_M001_C by Finnmap Consulting last updated on 6.3.2013 (Mäntynen & Viita 2013).

For numerical reasons the actual or potential gap opening was not feasible to be considered explicitly but a gap with similar water transport potential with thickness of 0.1 m was considered in all cases. The dimensions are shown in Figures 2-1 and 3-1. **The model size was reduced by half, on account of the vertical symmetry plane along the center line of the plug and the tunnel.**

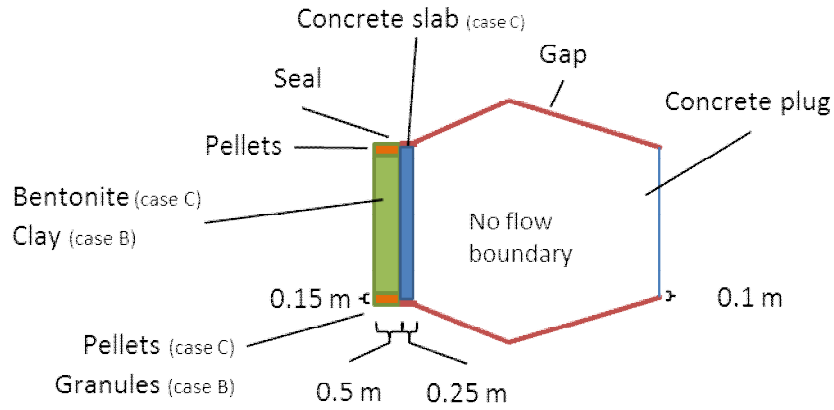


Figure 3-1. Dimensions of the seal system and assumptions regarding the gap between the concrete and host rock.

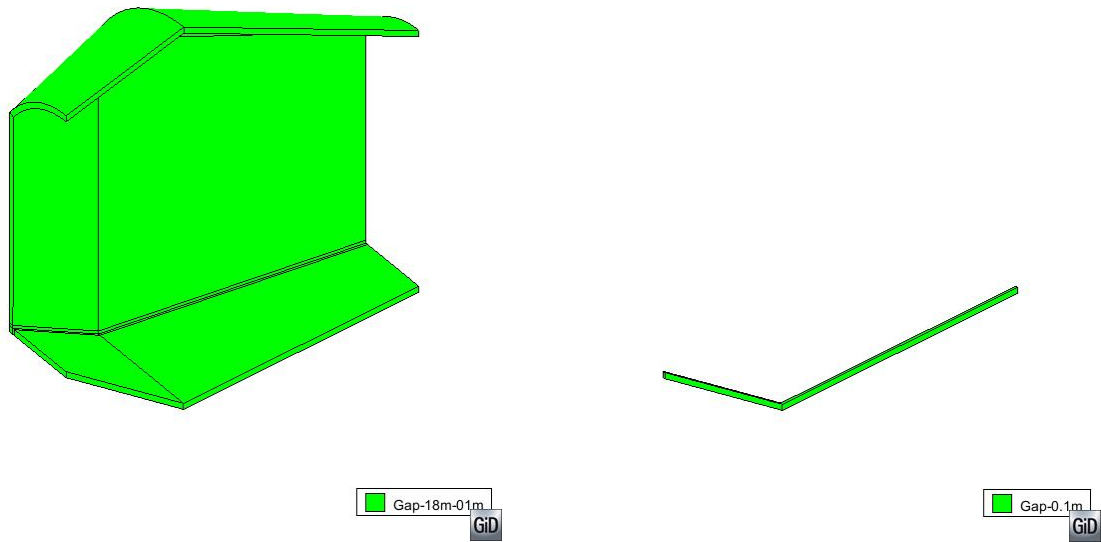


Figure 3-2. Geometries for design case A. Left: leakage scenario I (cases A_I and Ag_I). Right: leakage scenario II (cases A_II and Ag_II).

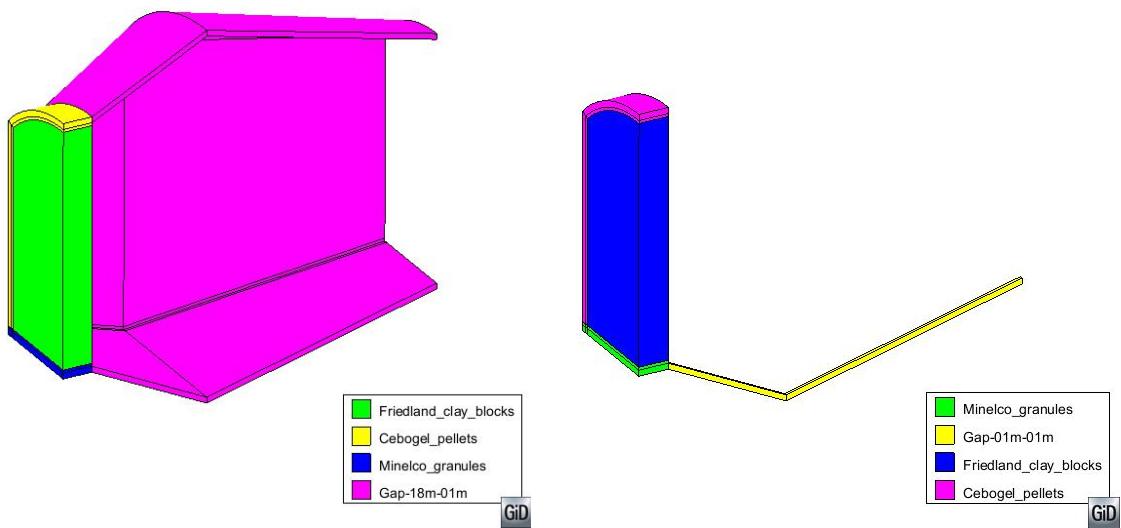


Figure 3-3. Geometries for design case B. Left: leakage scenario I (cases B_I and Bg_I). Right: leakage scenario II (cases B_II and Bg_II).

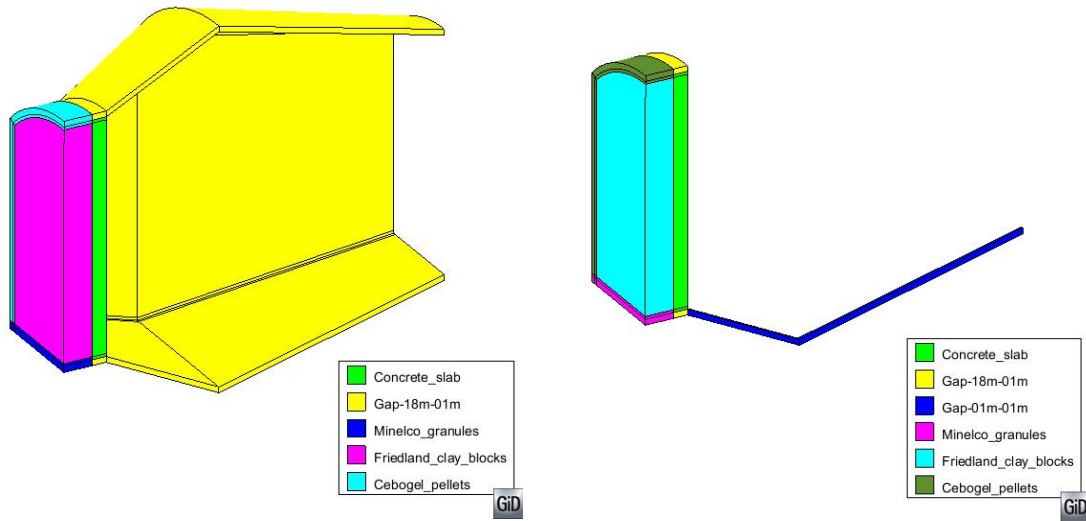


Figure 3-4. Geometries for design case B2. Left: leakage scenario I (case B2_I). Right: leakage scenario II (case B2_II).

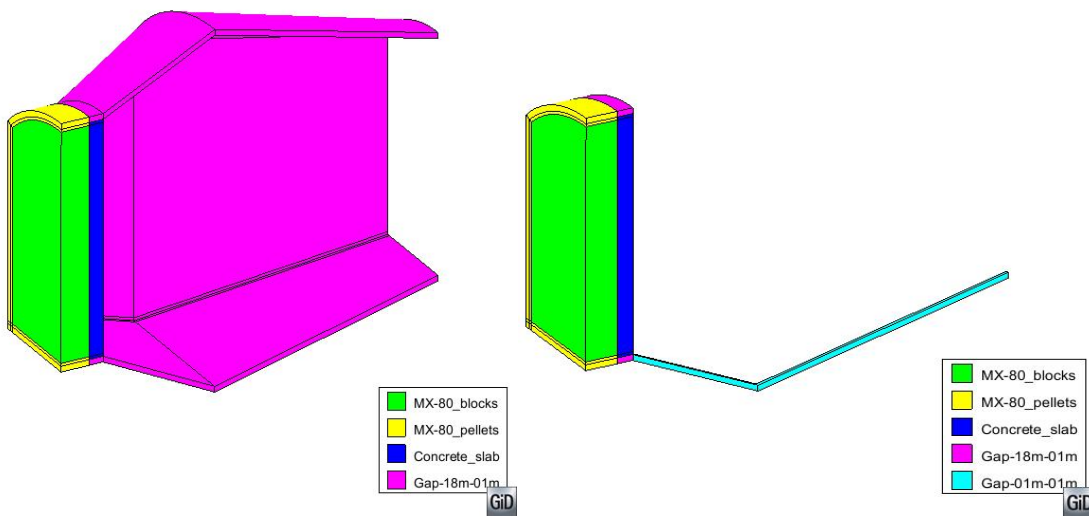


Figure 3-5. Geometries for design case C. Left: leakage scenario I (cases C_I and Cg_I). Right: leakage scenario II (cases C_II and Cg_II).

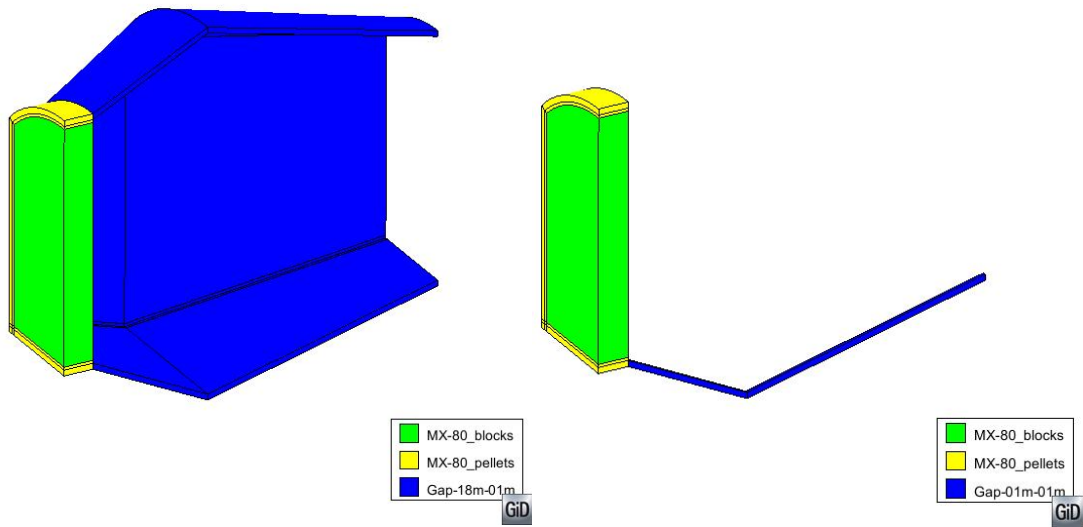


Figure 3-6. Geometries for design case C2. Left: leakage scenario I (case C2_I). Right: leakage scenario II (case C2_II).

3.1.3 Boundary conditions

A liquid pressure of 10 MPa was applied at the short end of the plug (case A) or on the seal (cases B and C), as illustrated with yellow in Figure 3-7. The surface of the gap facing the central tunnel (green in Figure 3-7) was assigned an atmospheric pressure of 0.1 MPa. **No-flow boundary conditions were prescribed on all other boundaries.**

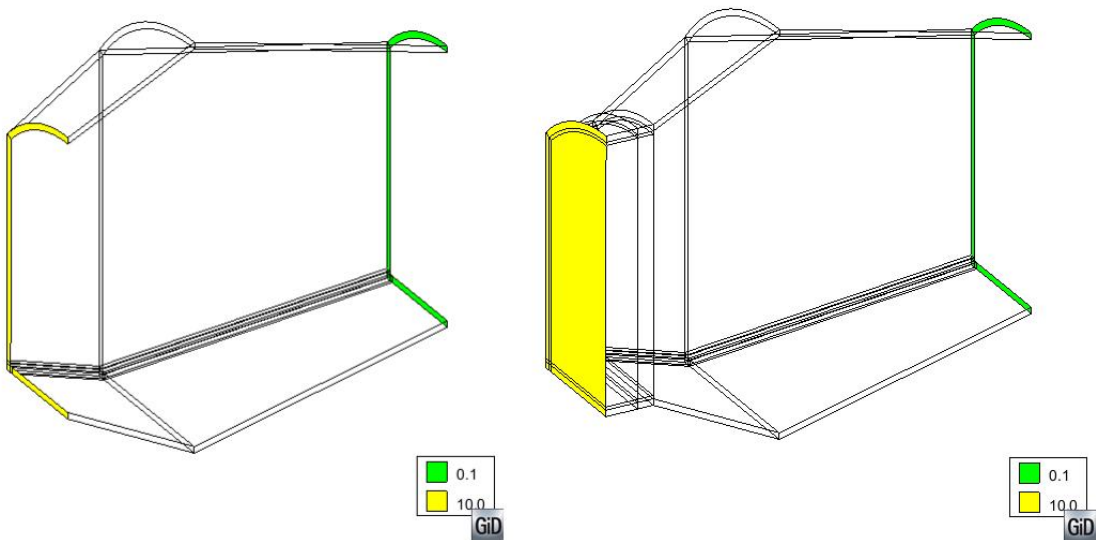


Figure 3-7. Boundary conditions (MPa) in case A (left) and cases B and C (right).

3.1.4 Initial conditions and fixed conditions

As the seal is saturated, an initial liquid pressure of 0.1 MPa was assigned to all materials. Gas pressure was fixed at 0.1 MPa (atmospheric pressure) and temperature at 20 °C, as during the operational period the temperature in the tunnels is assumed to be kept at about +20 °C (Haaramo & Lehtonen 2009).

Gravity was not employed in the base cases in order to study an even flow through the seal and the plug induced by the pressure difference. Incorporating gravity was found, in a few of the cases, to generate inflows at some boundary nodes at the surface of the gap facing the central tunnel (where liquid pressure is maintained at 0.1 MPa), as well as outflows on the seal surface (where liquid pressure is maintained at 10 MPa).

3.1.5 Material properties

The dry density of Friedland clay, Cebogel pellets and Minelco granules was determined based on data from homogenization tests (Johannesson et al. 2008), which indicated homogenized dry density values of about 1800 kg/m³ for Friedland clay, 1200 kg/m³ for Cebogel pellets and slightly less than 1300 kg/m³ for Minelco granules (Figure 3-8). As the initial dry density of the pellets and the granules in Posiva backfill is likely to be higher than in the homogenization tests, the selected values can be considered conservative. In the end, a dry density of 1290 kg/m³ was employed for Minelco granules, on account of published saturated hydraulic conductivity data available for this density (Posiva 2013a).

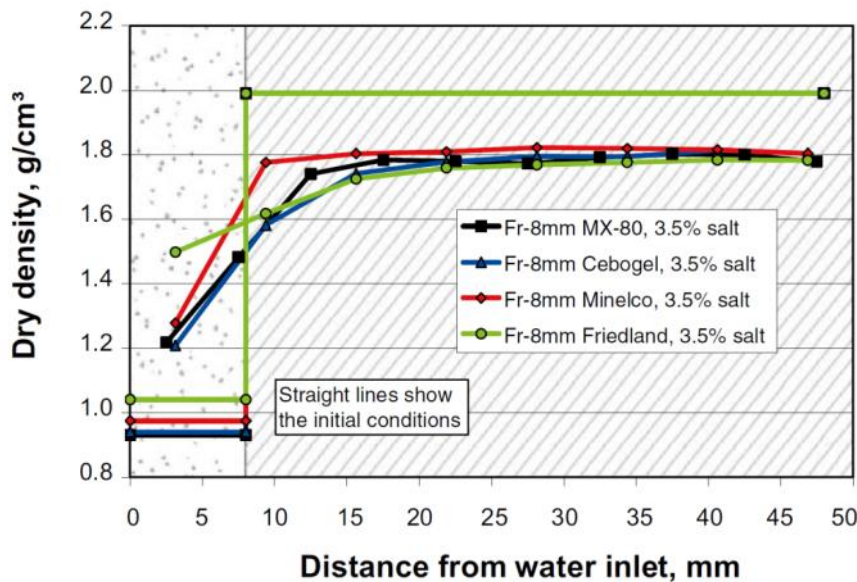


Figure 3-8. Dry density in homogenization tests, plotted as a function of the distance from the water inlet for four specimens made of Friedland blocks (Johannesson et al. 2008).

For MX-80, an overall void ratio level of 0.85 was chosen in order to yield a swelling pressure in the order of 3-4 MPa according to the swelling pressure relation presented by Åkesson et al. (2010a). The division in two different void ratio values for blocks and pellets, respectively, was based on the results from the backfill homogenization calculations presented in Åkesson et al. (2010b). These showed final void ratio distributions with a general difference in void ratio, between the inner and outer parts of the backfill, of slightly more than 0.2. With an overall void ratio level of 0.85 in Case C, this suggests that the final void ratios of homogenized blocks and pellets can be set to 0.75 and 0.95, respectively.

In CODE_BRIGHT, the flow rate in porous media is calculated using Darcy's law:

$$\mathbf{q}_l = - \frac{\mathbf{k} k_{r_l}}{m\eta} (\tilde{N}P_l - r_l \mathbf{g}) \quad (3-1)$$

where \mathbf{k} is the intrinsic permeability tensor of the medium, η is the dynamic viscosity of the liquid phase, \mathbf{g} is the gravity vector and k_{rl} is the relative permeability of the liquid phase (equal to 1 in saturated material).

The intrinsic permeability value for the gap material was calculated with an analytical solution, aiming for a flow of about 0.1 l/min through the plug (Appendix A). The gap permeability therefore changes with gap width, so the two leakage scenarios presented in Section 3.1.2 employ different intrinsic permeability values (e.g. in scenario II the gap width is 0.1 m, which is much smaller than in scenario I, so the intrinsic permeability for the 0.1 m wide gap is higher).

The intrinsic permeability values for the seal materials were selected from reported test data, for estimated homogenized densities of the materials. Sensitivity analysis of this parameter should be undertaken in future calculations.

Groundwater salinity in the repository is expected to be a little above 10 g/l (Pastina & Hellä 2010, Table 6-6). The saturated hydraulic conductivity values were therefore selected from measurements conducted with 10 g/l or higher saline water, depending on the availability of data. Higher salinity implies a slightly higher hydraulic conductivity, so no underestimation of the outflow should be incurred by this consideration.

The material properties in Table 3-2 are given in terms of the dry density ρ_d , void ratio e and/or the equivalent porosity f , and the intrinsic permeability k .

Table 3-2. *Material properties.*

Material	ρ_d (kg/m ³)	e/f (-)	k (m ²)	Reference for k
Gap (width: plug circumference, ca. 18 m)	-	-/0.020	5.99e-16	Analytical solution
Gap (width: 0.1 m)	-	-/0.020	1.08e-13	Analytical solution
Friedland clay blocks	1800	0.544/0.353	8.94e-20	Posiva (2013b)
Cebogel pellets	1200	1.36/0.577	1.13e-18	Schatz & Martikainen (2013)
Minelco granules	1290	1.17/0.538	5.65e-18	Posiva (2013a)
MX-80 blocks	1590	0.75/0.429	5.20e-21	Åkesson et al. (2010a)
MX-80 pellets	1430	0.95/0.487	1.80e-20	Åkesson et al. (2010a)
Concrete beam	-	-/0.135	1.00e-15	Åkesson et al. (2010a)

3.2 Results

The results of the simulations in terms of liquid pressures and their distributions in "the seal - plug - possible concrete beam" -system are presented in figures 3-9, 3-10 and 3-11. Figure 3-9 shows simulated liquid pressures in Case A that can be considered as reference design whereas figure 3-10 and 3-11 shows corresponding values for alternative designs (cases B_I, B_II, C_I, and C_II) and design variants (cases B2_I, B2_II, C2_I, and C2_II).

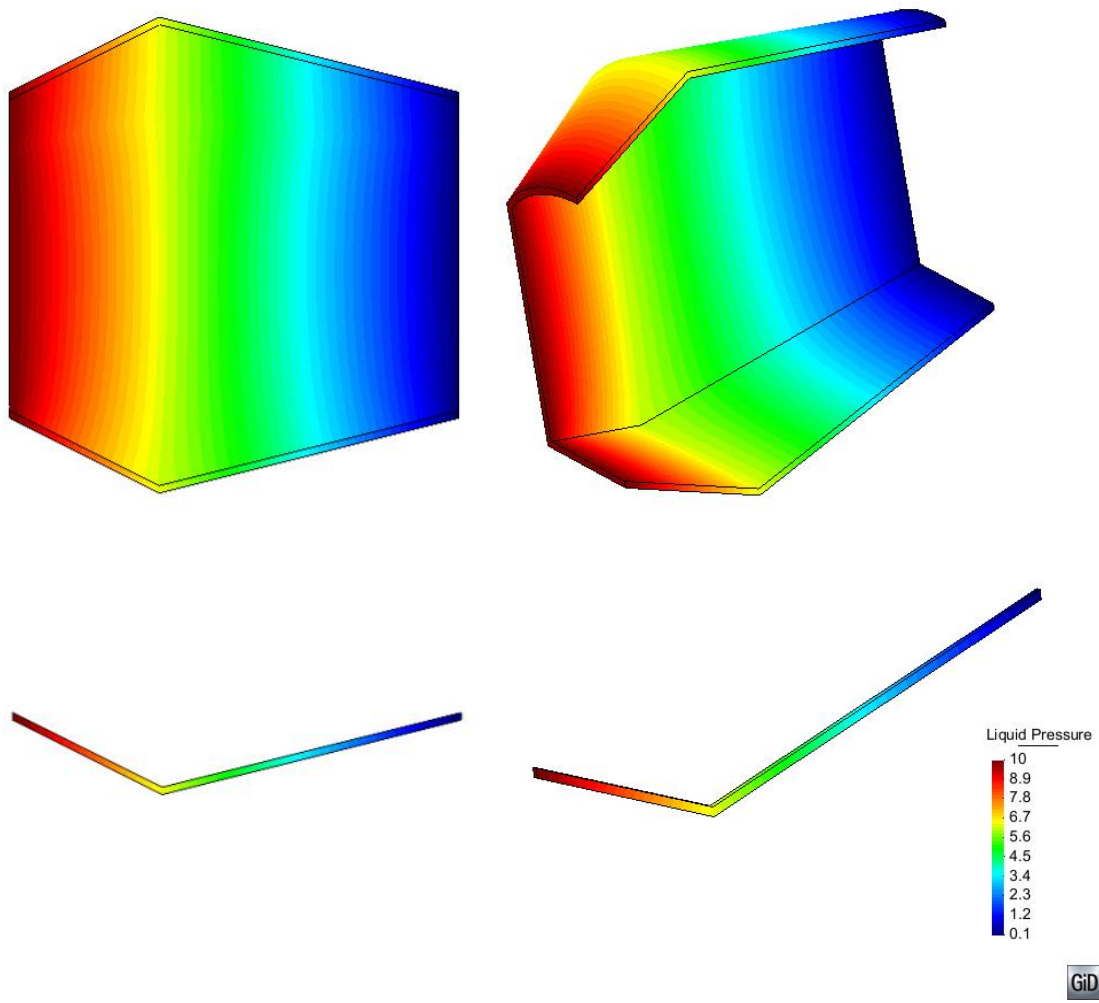


Figure 3-9. Liquid pressure in Poplu reference design.

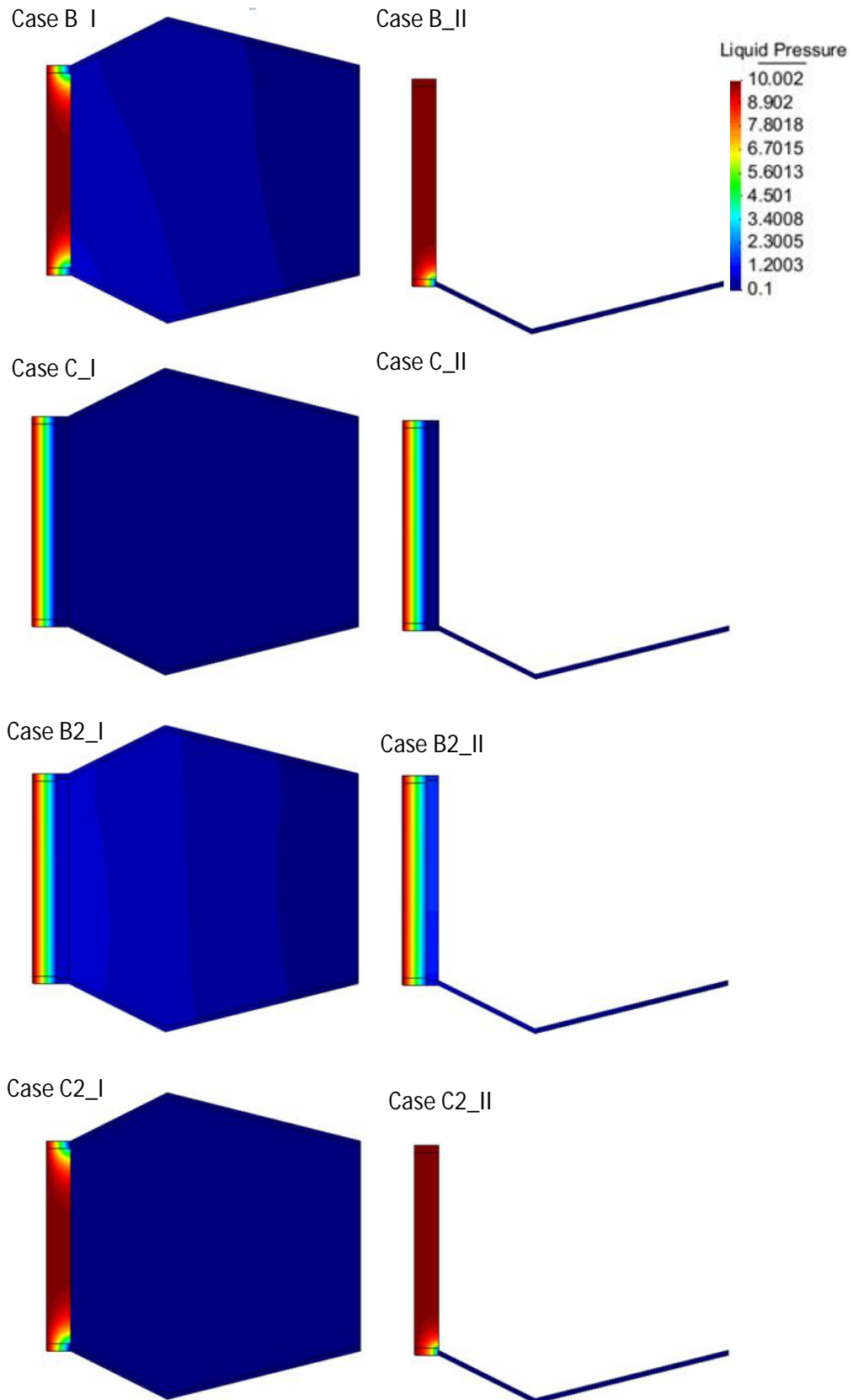


Figure 3-10. Longitudinal cross-sections of alternative designs.

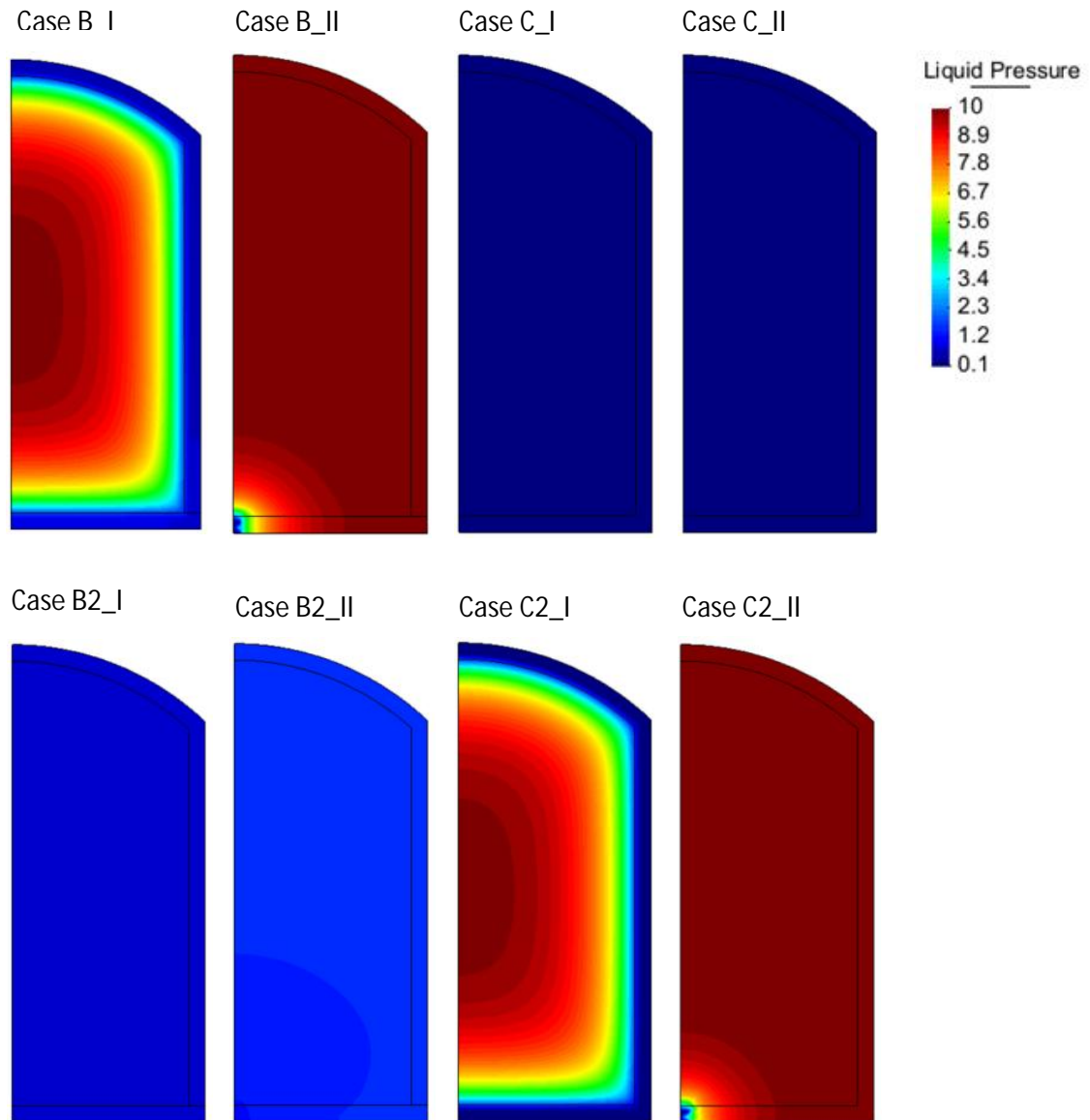
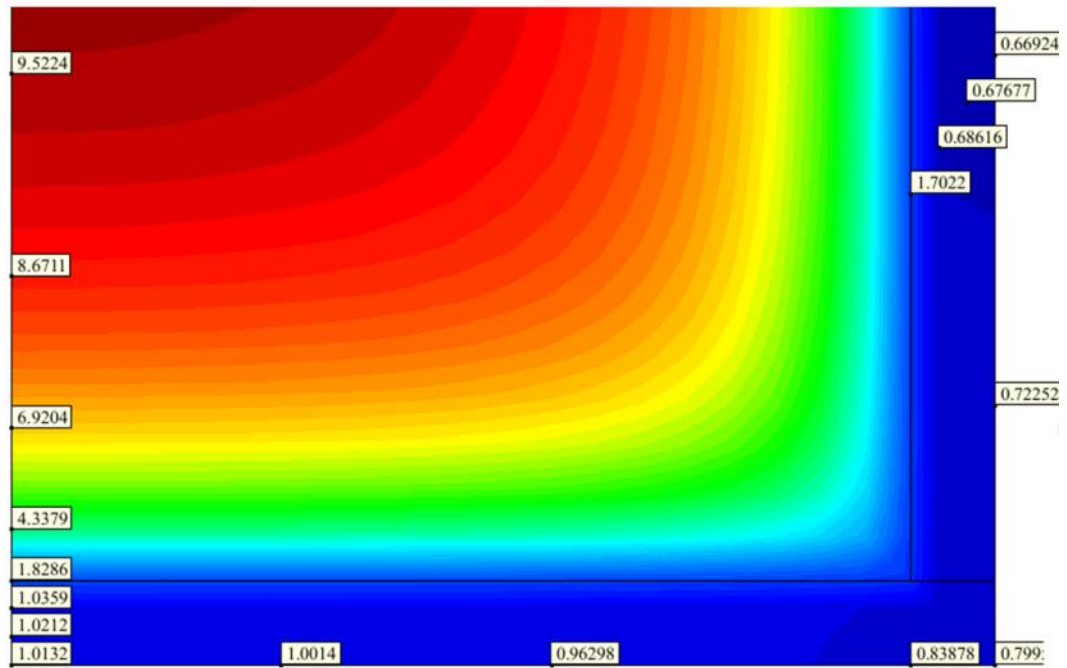


Figure 3-11. Crosstunnel cross-sections of alternative designs.

Figures 3-12 and 3-13 presents details to compare Friedland-Cebogel-Minelco backfill system to MX-80 backfill system i.e. cases B_I vs. C2_I and B_II vs. C2_II.

Case B_I



Case C2_I

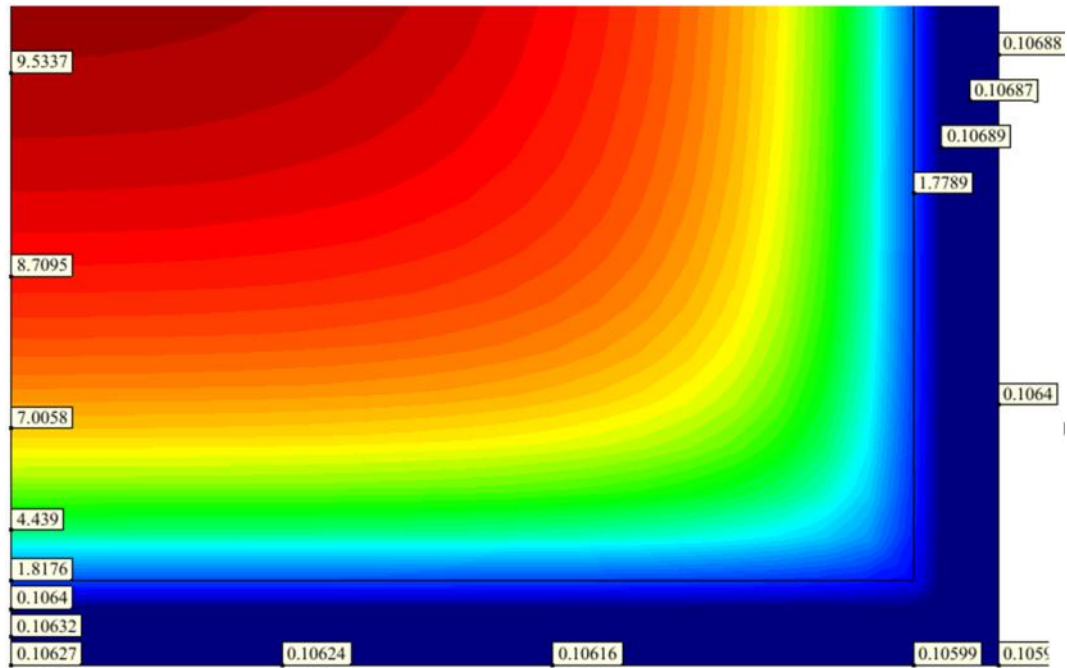
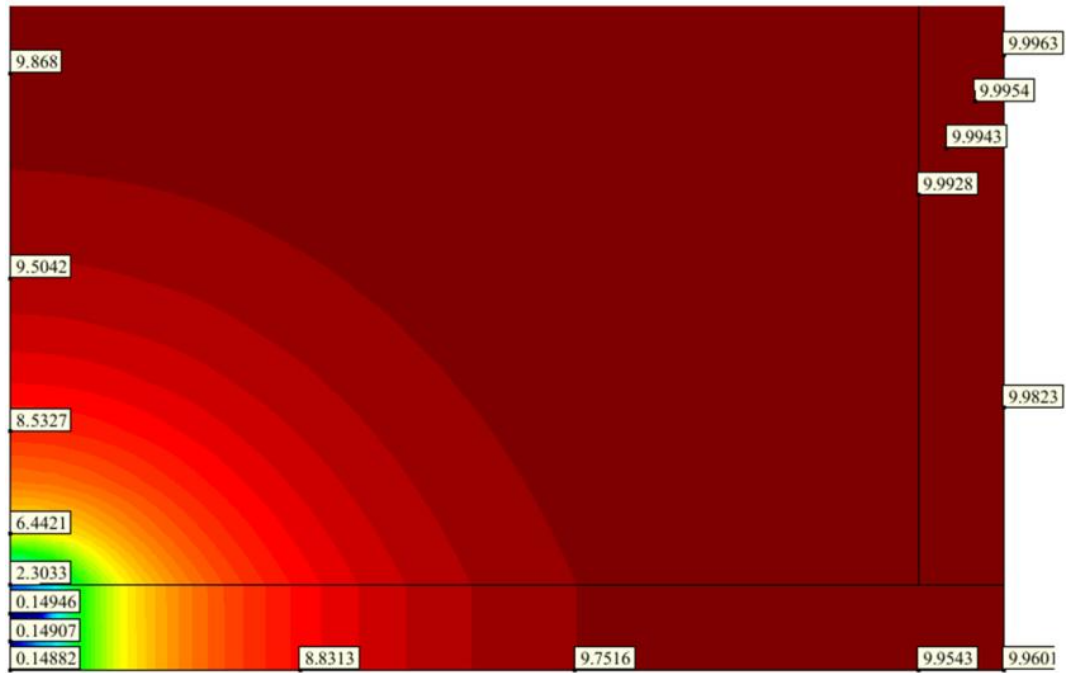


Figure 3-12. Details of liquid pressures in MPa at clay-concrete interfaces that are defected over the whole perimeter for Friedland-Cebogel-Minelco backfill (Case B_I) and MX-80 backfill (Case C2_I).

Case B_II



Case C2_II

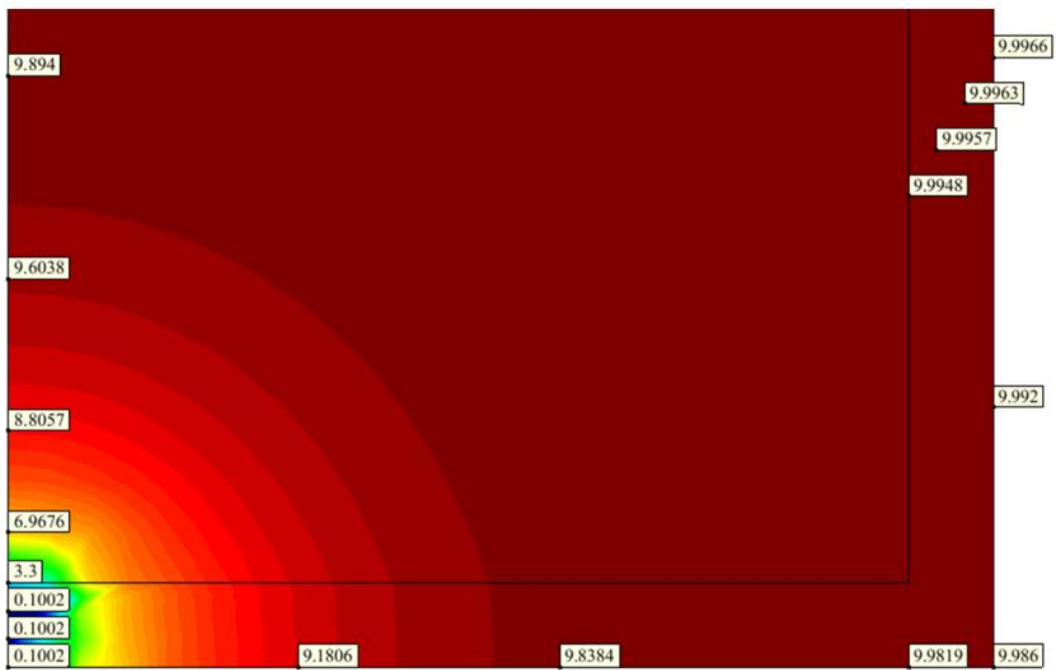
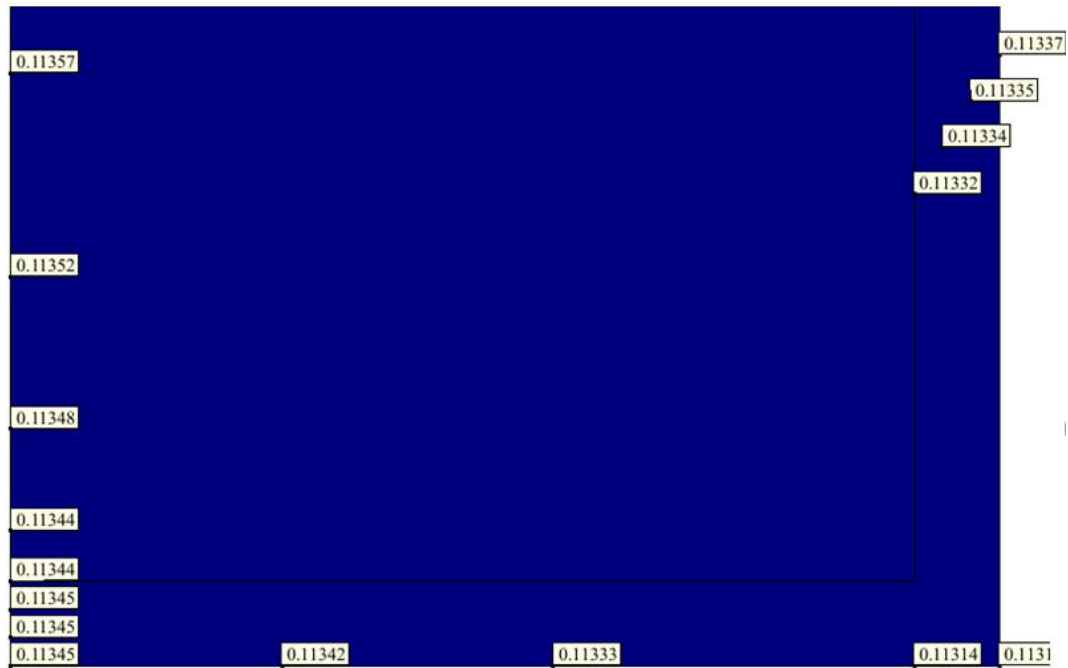


Figure 3-13. Details of liquid pressures in MPa at clay-concrete interfaces that are defected over a 10 cm wide section for Friedland-Cebogel-Minelco backfill (Case B_II) and MX-80 backfill (Case C2_II).

Moreover, Figure 3-14 illustrates the anticipated effect of defect size for a MX-80 backfill system.

Case C_I



Case C_II

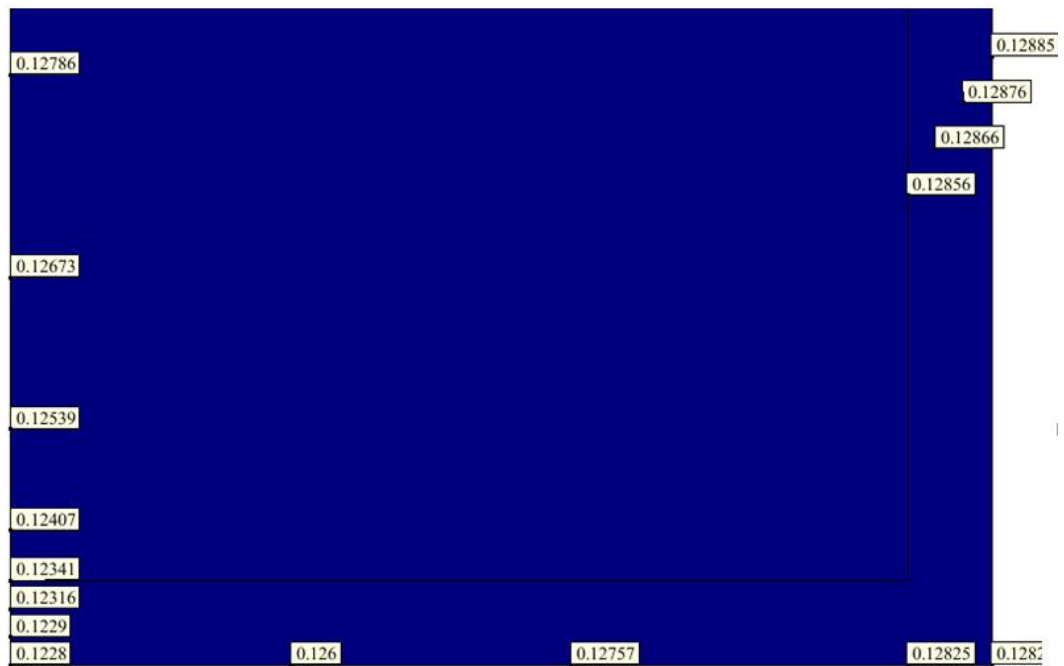


Figure 3-14. Details of liquid pressures in MPa at clay-concrete interfaces for a MX-80 backfill system in the case of and interface defected over the whole perimeter (Case C_I) and over a 10 cm wide section (Case C_II).

The resulting flow rates through the plug systems as steady-state outflows from the gap surface facing the central tunnel are presented in Table 3-3 for the cases without gravity and in Table 3-4 for cases with gravity.

Table 3-3. Simulated plug outflows for design cases A, B, B2, C and C2 (no gravity incorporated).

Case	Outflow (l/min)	Case / Case A (%)	Seal material	Gap width
A_I	0.0917	100	-	Plug circumference
A_II	0.0949	100	-	0.1 m
B_I	0.00544	5.94	Friedland-Cebogel-Minelco backfill	Plug circumference
B_II	0.000468	0.493	Friedland-Cebogel-Minelco backfill	0.1 m
B2_I	0.00643	7.01	Friedland-Cebogel-Minelco backfill + concrete beam	Plug circumference
B2_II	0.00597	6.30	Friedland-Cebogel-Minelco backfill + concrete beam	0.1 m
C_I	0.000128	0.140	MX-80 + concrete beam	Plug circumference
C_II	0.000116	0.122	MX-80 + concrete beam	0.1 m
C2_I	0.0000665	0.0725	MX-80	Plug circumference
C2_II	0.00000148	0.00156	MX-80	0.1 m

Table 3-4. Simulated plug outflows for design cases A, B and C (gravity incorporated).

Case	Outflow (l/min)	Case / Case A (%)	Seal material	Gap width
Ag_I	0.0917	100	-	Plug circumference
Ag_II	0.0949	100	-	0.1 m
Bg_I	0.00545	5.95	Friedland-Cebogel-Minelco backfill	Plug circumference
Bg_II	0.000470	0.495	Friedland-Cebogel-Minelco backfill	0.1 m
Cg_I	0.000116	0.126	MX-80 + concrete beam	Plug circumference
Cg_II	0.000121	0.128	MX-80 + concrete beam	0.1 m

Incorporating gravity was found, as already said, in a few of the cases, to generate inflows at some boundary nodes at the surface of the gap facing the central tunnel (where the liquid pressure boundary condition is 0.1 MPa), as well as outflows on the seal surface (where the liquid pressure boundary condition is 10 MPa). The results with and without gravity differ by very little, the most notable difference being the outflows in the two leakage scenarios of case C.

3.3 Comparison of main design cases

3.3.1 Effect of clay material

For the full circumference sized defect with Friedland-Cebogel-Minelco backfill (design case B_I), the outflow decreases by a factor of approximately 17 compared to case without clay material (Case A_I) and with MX-80 seal (Case C2_I) the estimated decrease in the outflow is by a factor 1380. For a 0.1 m wide defect the decreases are roughly an order of magnitude larger and the relative difference in outflow between these two backfill systems is roughly four (4) times bigger.

With MX-80 bentonite as the seal and a concrete beam placed between the seal and the plug (design case C), the outflow is reduced by a factor of approximately 715 compared to case A. Compared to design case B, the outflow in design case C is reduced by a factor of about 42.

Overall, it can be summarised that when adding a seal material to face any potential defect in concrete (Cases B), the effect of these materials is that the flow rate through the defect is being reduced at least with an order of magnitude. In the case of less permeable seal material (Cases C2) an even further reduction of roughly of two orders of magnitude can be expected. The absolute reduction in the flow through rate is not directly comparable to the ratios of permeabilities of defect to that of backfill material (especially pellets), but less by a factor far less than an order of magnitude. However, the difference in flow through rates between reference and alternative backfill materials is proportional to their ratio of permeability. These conclusions are made based on assessments without clay penetration into an empty gap but with configuration dependent stresses around the defect. They suggest dominant dependence of the flow rate ratio on the ratio of permeabilities in a way similar to that of the theoretical considerations presented in Appendix B. In the numerical simulations the deviation is by a factor <1 whereas in the theoretical considerations such a deviation from a pure permeability ratio is by a factor >1 . These deviation factors are though several orders of magnitude smaller than the permeability ratios relevant in this connection.

Thus, these simulations suggest that in the case of no backfill material the high hydrostatic pressure will be reduced to atmospheric pressure within the length of the potential defects. Should a less permeable material be used to face any potential defect, the reduction in the hydrostatic head will take place within the less permeable material as opposed to within the concrete part of the plug - the lower the permeability in backfill the bigger the reduction in the hydrostatic head within the backfill. Consequently, in case of introducing a less permeable material a smaller hydrostatic head over the potential defects in the concrete part of the plug can be expected, yielding a lower flow through rate and better watertightness.

3.3.2 Effect of concrete beam

The foreseen effect of concrete beams is that they make the supply of water to the potential defects easier, as it can be seen when comparing the concrete beams cases with full perimeter defect to 0.1 m wide defects: the outflow rates are practically the same in Cases B2_I and B2_II as well as in Cases C_I and C_II. The impact of backfill permeability remains the same as described in Section 3.3.1.

3.3.3 Effect of defect width

The effect of a potential defect in the concrete part of the plug is roughly directly comparable to its width in the cases when backfill is in direct contact with the concrete part. However, should there be concrete beams in between clay backfill and the concrete part of the plug, the effect of the defect width is suggested to vanish.

It should be pointed out that the value of the results is limited by the simplified boundary conditions made:

1. A free water surface is applied on the boundary to the backfill, which means that the influence of the bulk of the backfill on the water supply to the plug is not considered
2. Water flow in the rock is neglected or assumed to be lumped into water flow through the defect.

4 PREDICTION OF MECHANICAL INTEGRITY

4.1 Simulated cases and scenarios

The mechanical properties and behaviour of the rock mass together with the concrete part of the plug was simulated with 3DEC 5.00 (Itasca Consulting Group (2012)), which is a jointed polyhedral discrete element software featuring finite-elements for sections considered continuum.

The following three scenarios were simulated to assess the impacts of the uncertainties expected to be the most noteworthy.

- Case 1.* (Overly) Homogeneous rock mass: The same fully VGN lithology is used as in previous assessments, as well as the pilot hole observations (i.e. does not include OL-BFZ297).
- Case 2.* (Overly) Heterogeneous rock mass: A change in lithology from VGN to PGR is included but its location is stylised such that its impact would be the worst with respect to the load transferred from the plug to the rock mass. Furthermore, OL-BFZ29 is included but its location is changed to a location that would be as adverse as possible but would still fulfil the rock suitability criteria.
- Case 3.* (Overly) Heterogeneous rock mass with pessimistic parameter values: Case 2 with a decrease of 60% in the respective tensile strengths.

The features included in the model are described in Section 2.2 together with the parameter values in Tables 2-1 to 2-4.

Cases 1 and 2 include results where displacements have been reset prior to implementing water pressure.

Earlier simulations detailed in WR 2009-38 defined the rock mass tensile strength according to the Hoek-Brown criterion, which is not employed in this connection when three joint sets are not present and the quality of the rock is good. Hence the tensile strength parameters are much higher in these simulations and large plastic tensile strains are not observed in the results.

4.2 Results

The main aim of these calculations was to study the load caused by the fully saturated backfill at the depth of c. 400 m at the backfill side face of the plug (assumed to be 10 MPa) which induces a compressive stress field to this face.

Figure 4-1 presents the locations of the horizontal and longitudinal cross-section locations used in presenting the results.

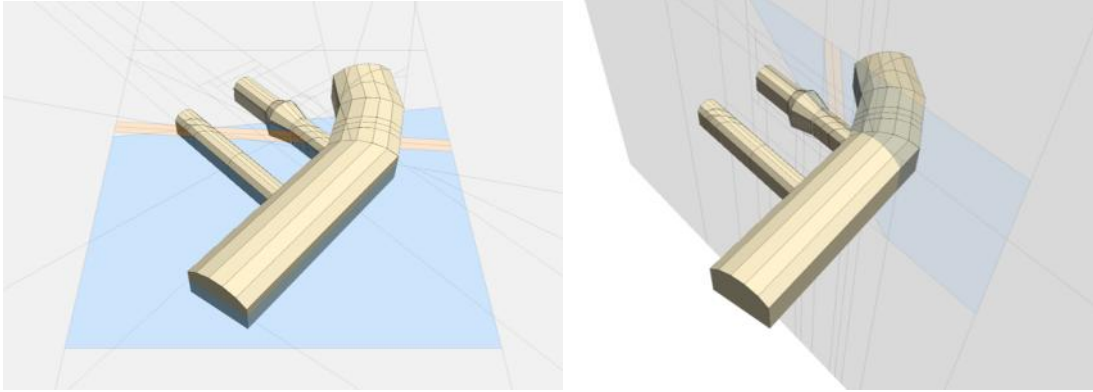


Figure 4-1. Horizontal and longitudinal section locations.

4.2.1 Displacements

Figure 4-2 presents the simulated displacements.

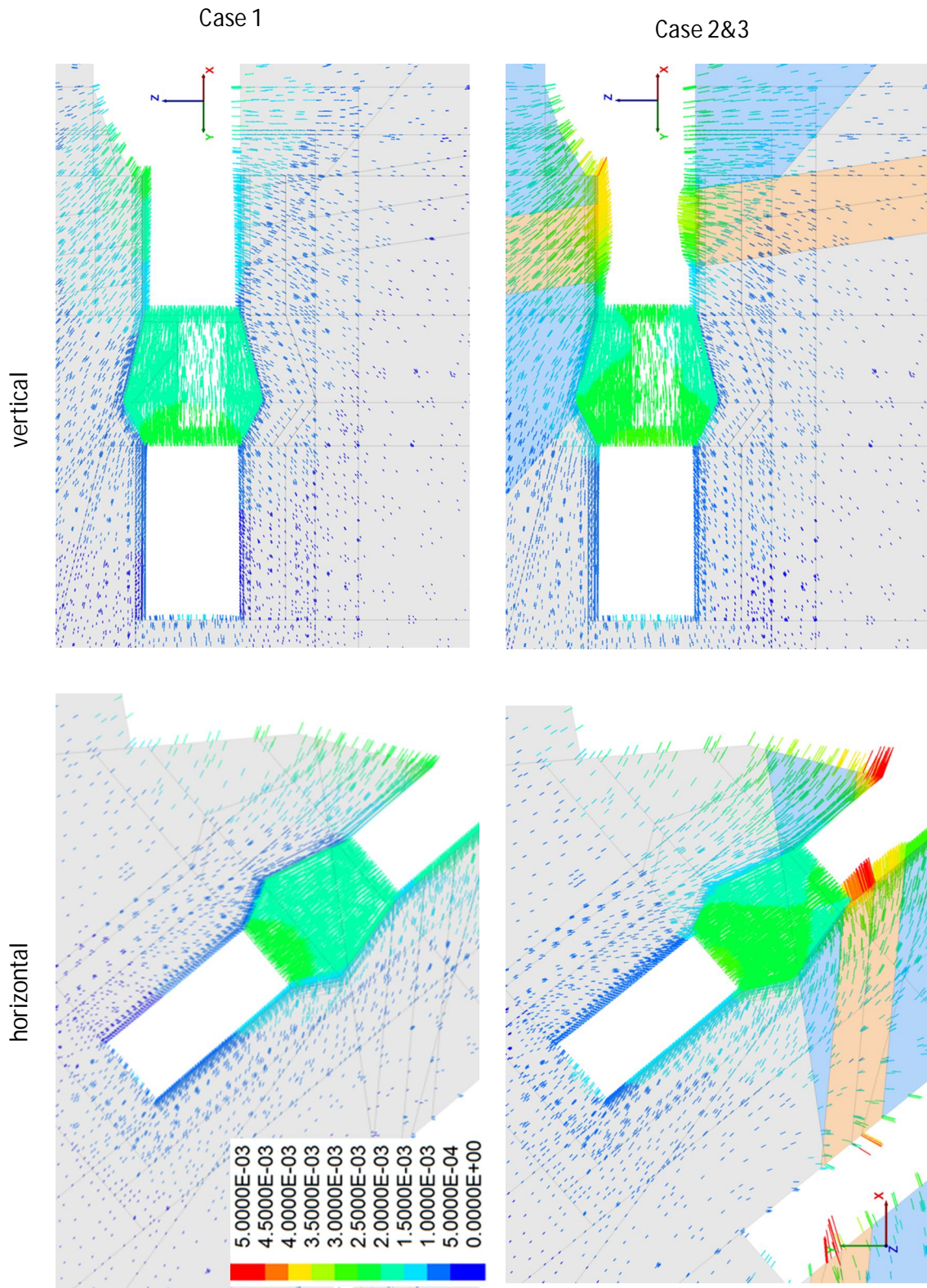


Figure 4-2. Displacements in [m] after cavity pressurisation. Pressurisation is from the left in all graphics.

The differences between the scenarios assessed are of the order of a few millimetres maximum in the rock and less than one millimetre in the concrete part of the plug. The differences in the rock mass are explained by the displacements after the excavation of the drift in cases 2 and 3. This is illustrated in Figure 4-3, presenting displacements for cases 2 and 3 before and after cavity pressurisation.

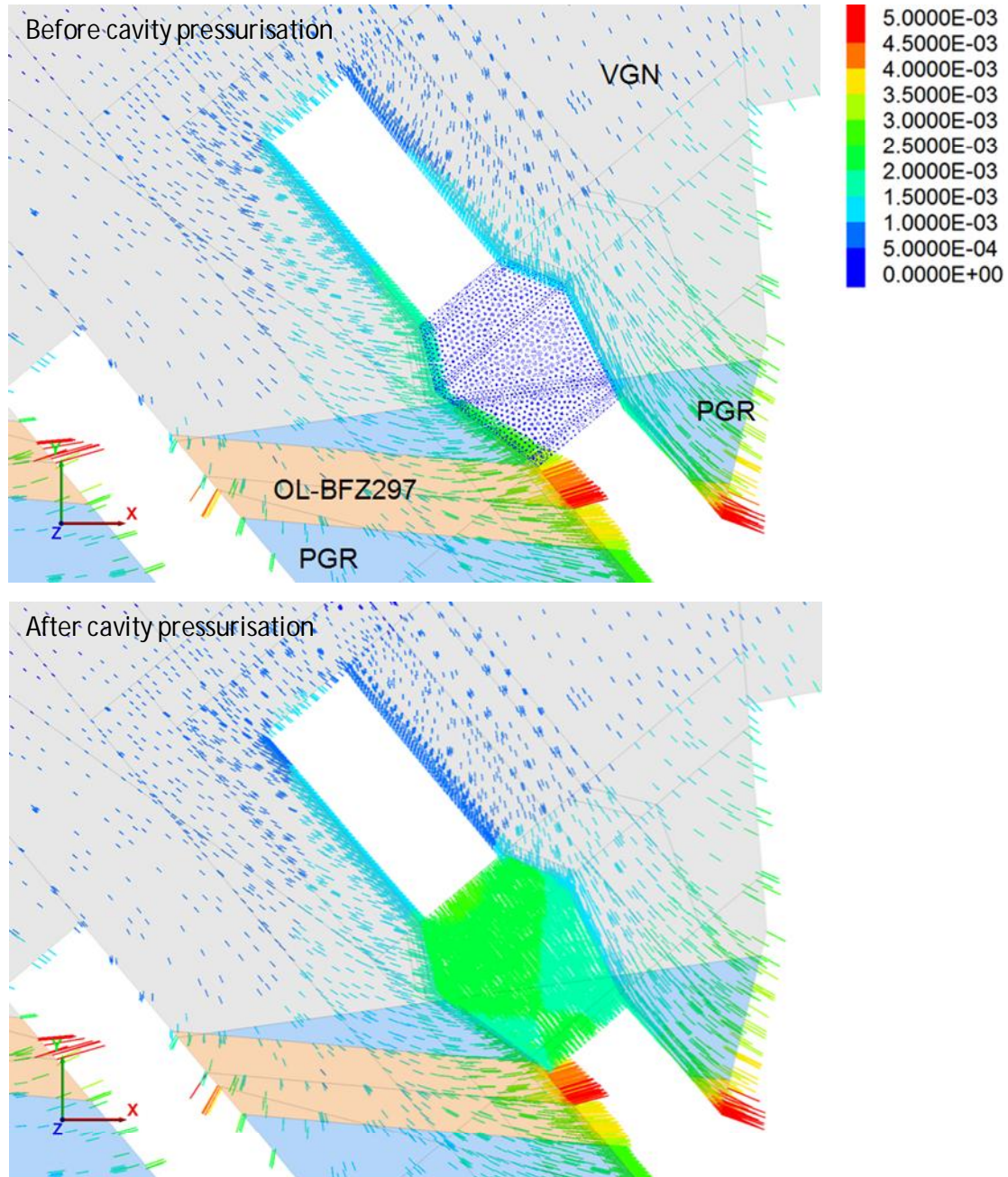


Figure 4-3. Displacements in [m] for cases 2 and 3 before and after cavity pressurisation.

To estimate the changes in displacements, the displacements occurring immediately after cavity excavation are removed and then actual displacement is presented in Figure 4-4.

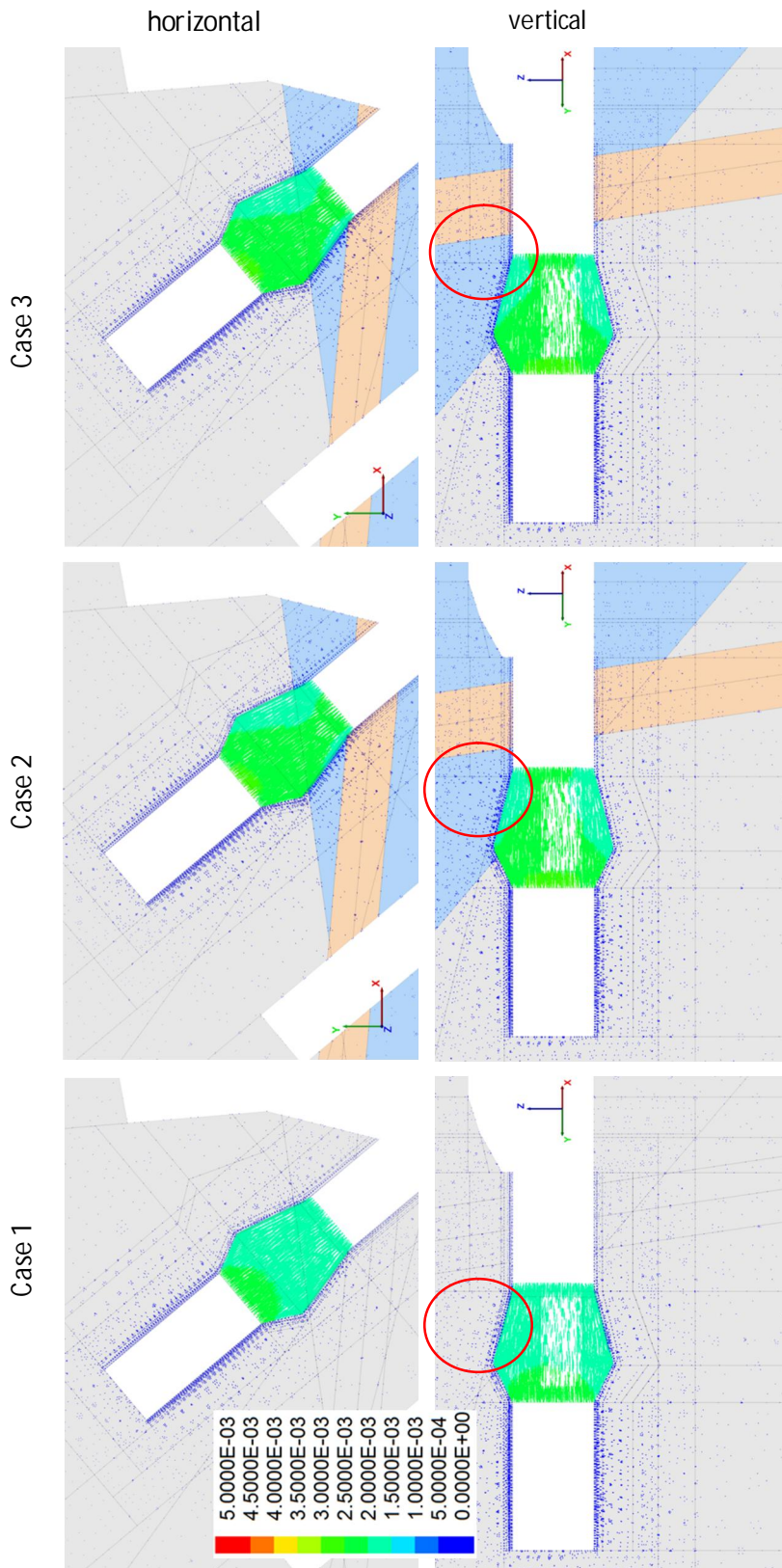


Figure 4-4. Calculated displacements in [m] after cavity pressurisation. The displacements occurring immediately after cavity excavation are removed. Red circle = displacements.

When comparing displacements in the rock mass inside the red circles in case 1 to those of cases 2&3 visible in the horizontal cross-sections of Figure 4-4, there appears small differences that are

not that clearly visible in Figure 4-2. These differences correlate with the differences in the concrete part of the plug (inside the red circle in Figure 4-4).

The most obvious conclusions based on simulated displacements are:

1. The concrete plug can be expected to deform more than the rock mass. This is because Young's modulus for concrete is much lower than that of VGN or PGR rock mass.
2. Deformations of the concrete plug are symmetric should the rock mass be homogeneous and asymmetric in case the rock mass is heterogeneous e.g. in terms of lithology or appearance of fractures. The largest deformations in the concrete part that can be expected are 2.5-3 mm located at the side facing the pressurised cavity.
3. Heterogeneities in the deformation of the concrete part of the plug correlate with the displacements appearing in the rock mass in the vicinity of a fracture. That is, fractures in the rock mass induce local displacements in the rock mass under load that further induce local deformations in the concrete part of the plug. Should fractures appear in a symmetric manner, the deformations in the concrete part of the plug appear symmetrically.

Regarding the displacements in the rock mass, the changes due to cavity pressurisation can be expected to remain in the immediate vicinity of the drift. Some of these changes are due to the increased pressure in the cavity inducing an order of one millimetre backward movement of cavity walls that initially occurred due to relaxation of stresses after cavity excavation. These locations are denoted with red ellipses in Figure 4-5.

Moreover, a deformation of rock mass of similar order of magnitude can be expected in the locations closer to the longer wedge surfaces of the concrete part of the plug once the cavity is pressurised. These locations are indicated with black ellipses in Figure 4-5. This is because of the way the concrete part transfers the mechanical load from the simulated backfill through the longer wedge surfaces to the rock mass. The rock mass is assumed very stiff in this connection so that the deformations are expected to remain small and very local. The asymmetry of both red and black circles coincides with the alignment of the computational grid to such an extent that its influence cannot be excluded.

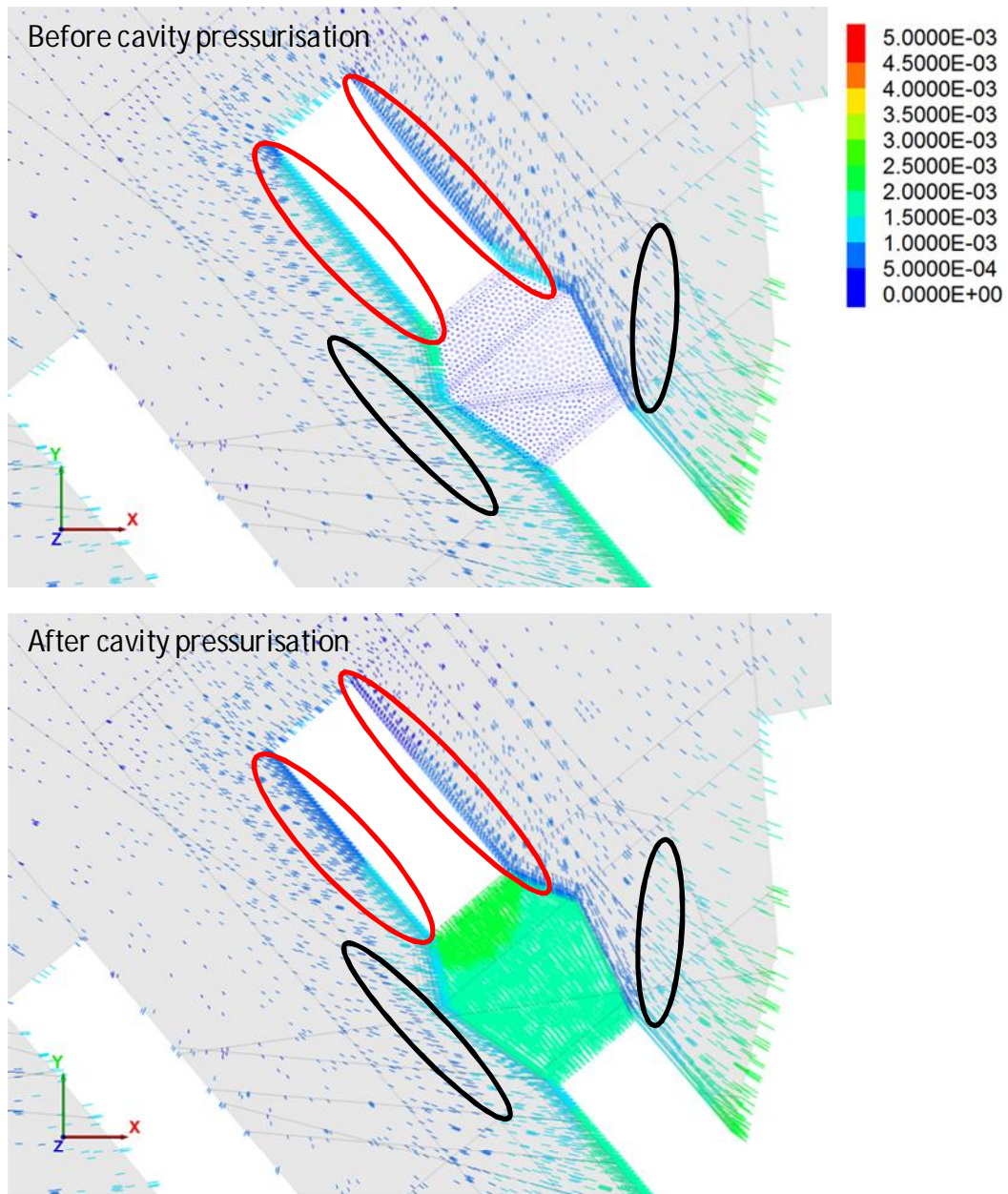


Figure 4-5. Calculated displacements in [m] for case 1 before and after cavity pressurisation. Red ellipses= movement of cavity walls, Black ellipses = deformation of rock mass.

4.2.2 Maximum and minimum principal stress

Figure 4-6 presents the simulated maximum principal stresses. It can be seen that in the concrete part of the plug there are areas of lower stresses in the more heterogeneous cases with an intersecting fracture highlighted with red circles. These locations coincide with those of larger displacements (see e.g. Figure 4-4). The differences in rock mass are more noticeable. Namely, stresses at the rock-concrete interface appear symmetrical in the homogeneous case and asymmetrical and locally higher in heterogeneous cases as denoted by black ellipses in Figure 4-6. The stresses are lower at more distant locations for the heterogeneous cases since displacements at

the fracture can be expected to relax some of stresses around the area denoted with a grey dashed ellipse. Moreover, variation of stresses typically referred to as checkerboard pattern in cases 2 and 3 in location framed with a black dotted line is often related to numerical solution indicating nothing of actual physics. Variation in cases 2 and 3 appears around the value estimated for the case 1.

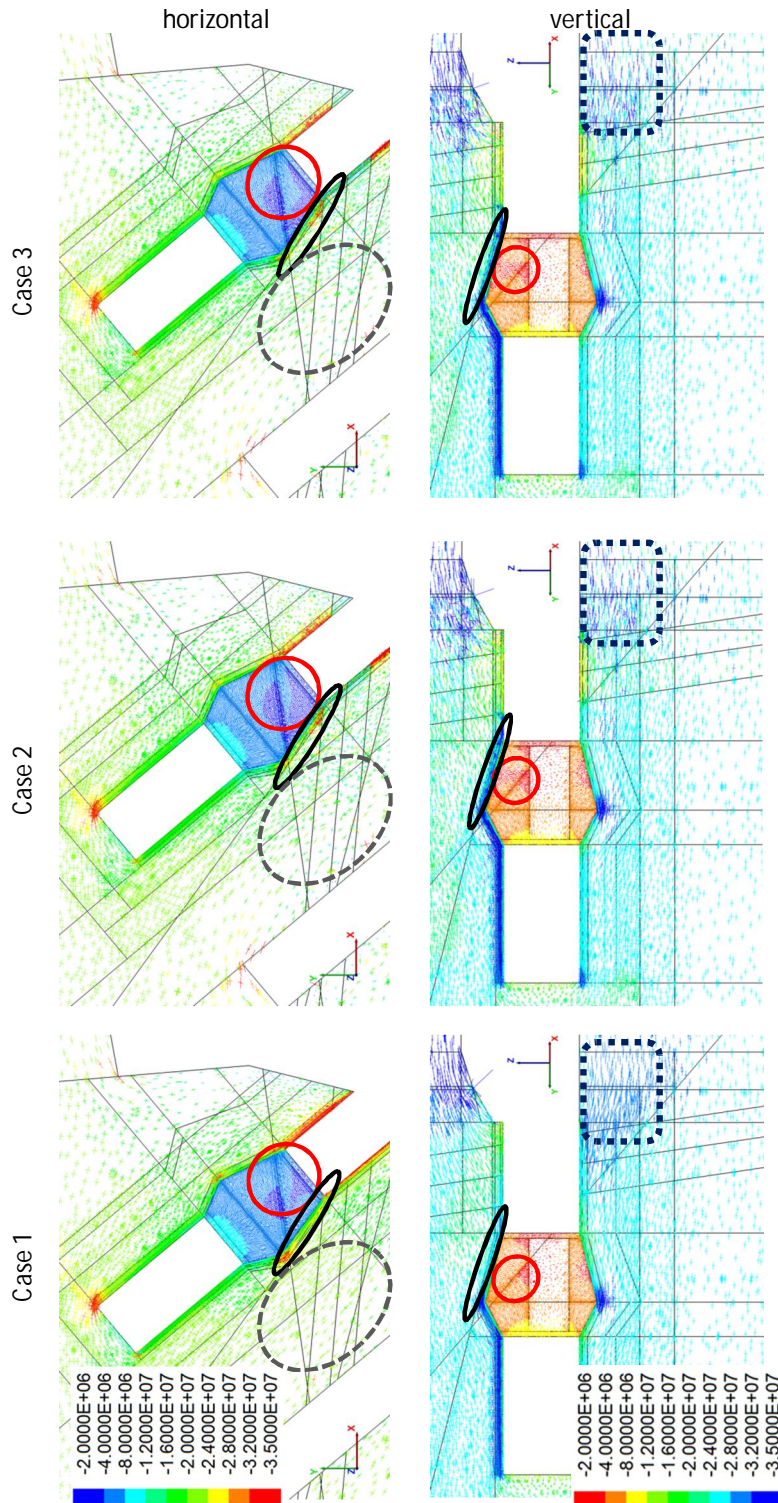


Figure 4-6. Maximum principal stresses in [Pa] after cavity pressurisation $\sigma_1 < 0$ refers to compression. Red circles=areas of lower stresses, Black ellipses=stresses at the rock-concrete interface, Black dotted ellipses=stresses are lower at more distant locations, Black dotted areas=variation of stresses often related to numerical solution indicating nothing of actual physics.

Minimum principal stresses are presented in Figure 4-7. As a conclusion, the expected stress fields are more heterogeneous in more heterogeneous conditions as well.

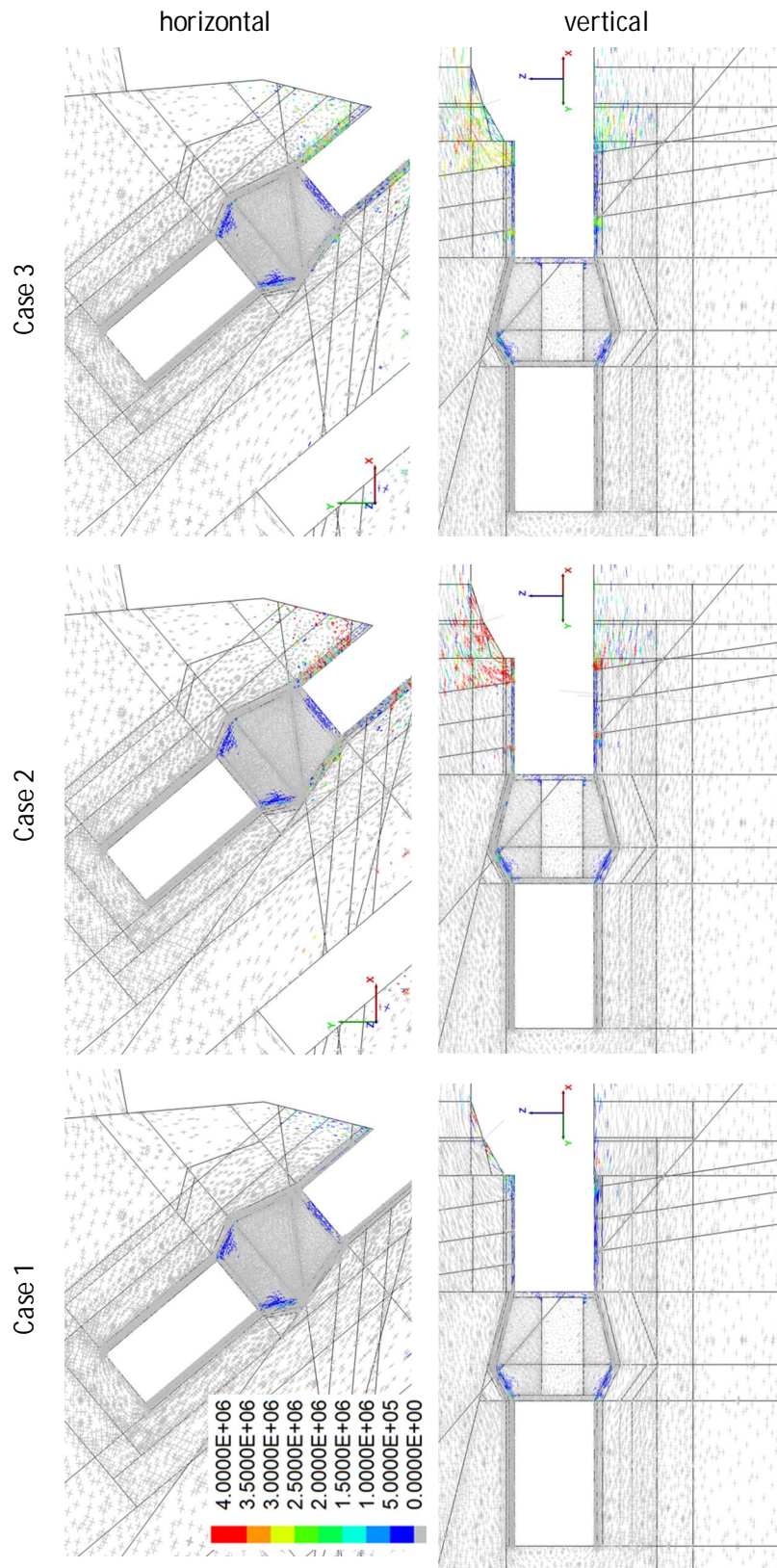


Figure 4-7. Minimum principal stresses in [Pa] after cavity pressurisation. $\sigma_1 < 0$ refers to compression.

5 SUMMARY

5.1 Watertightness

The plug area is defined here to include the concrete part, the potential seal layer and the rock mass within the slot at the distance of a few decimetres from the concrete plug.

The rate at which water may flow from the pressurised cavity past the plug is directly proportional to:

- i. permeability of the system including potential defects especially at the interface between the concrete and rock mass and
- ii. the width of the potential defect that provides a continuous flow path past the plug.

Clay as a low permeability material reduces the potential flow rates past the plug. The lower the clay permeability, the lower the flow rate past the plug. Since clays will be introduced as compacted blocks and pellets filling the gaps into which blocks cannot be placed, the permeability of the outermost parts in contact with the interface between the concrete part of the plug and rock mass depends on a) the swelling capacity of blocks to compress the pellets to a higher density and b) permeability of the fully water saturated and compressed pellets layer.

The effect of the concrete beams in contact with the plug is to redistribute the water potentially flowing in channels in backfill to the potential defects in the concrete-rock mass interface. This way concrete beams potentially makes the impact of smaller defects larger.

No leakages are expected since grout and bentonite tape will be used to seal potential defects at the circumferential concrete-rock mass interface. Ultimately, it is suggested that no clay as a seal or backfill would be used in the POPLU experiment to get direct evidences of the watertightness of the plug. The assessments presented in this report strongly support the assumption that water saturated clay would reduce the water flows past the plug to a negligible level anyway.

5.2 Mechanical integrity

The expected maximum displacements are roughly 3 mm in the concrete part of the plug whereas the rock mass is expected to have displacements of similar magnitude towards the drift and in the proximity of fractures slightly more.

Water pressure in the cavity is transferred into the rock mass through the longer wedge surfaces of the concrete part of the plug. The more heterogeneous the rock mass (in terms of lithology and fractures), the more uneven the stress field in the vicinity of the slot. In addition, changes in lithology and presence of fractures in the rock mass at the region in the opposite side of the plug in comparison to the pressurised cavity, induce higher displacements to the immediate vicinity of the load transferring surfaces.

To conclude, no material failures are expected even if there would appear undetected features at the most critical locations. Changes due to plug pressurisation can be measured in the concrete part of the plug as well as in the rock mass. This way the mechanisms of the transfer of the mechanical load through the plug to the rock mass can be validated.

REFERENCES

- Åkesson, M., Börgesson, B., Kristensson, O. (2010a). Sr-Site Data report. SKB Technical report TR-10-44.
- Åkesson, M., Börgesson, B., Kristensson, O., Dueck, A., Hernelind, J. (2010b). THM modelling of buffer, backfill and other system components. Critical processes and scenarios. SKB Technical report TR-10-11.
- Haaramo, M., Lehtonen, A. (2009). Principle plug design for Deposition Tunnels. Posiva Working Report 2009-38.
- Johannesson, L.-E., Sandén, T., Dueck, A. (2008). Deep repository – engineered barrier system. Wetting and homogenization processes in backfill materials. Laboratory tests for evaluating modeling parameters. SKB R-08-136.
- Itasca Consulting Group, Inc. (2012) *FLAC3D – Fast Lagrangian Analysis of Continua in Three-Dimensions, Ver. 5.0*, Minneapolis, Itasca.
- Mäntynen, A., Viita, I. (2013). Posiva Oy. Loppusijoitustilan tulppa. POPLU testitulppa. Finnmap Consulting.
- Olivella, S., Carrera, J., Gens, A., Alonso, E.E. (1994). Non-isothermal multiphase flow of brine and gas thorough saline media. *Transport Porous Media*, 15: 271–293.
- Olivella, S., Gens, A., Carrera, J., Alonso, E.E. (1996). Numerical formulation for a simulator (CODE-BRIGHT) for the coupled analysis of saline media. *Eng. Comput.*, 1: 87–112.
- Pastina, B. & Hellä, P. (eds.) 2010. Models and data report 2010. Eurajoki, Finland: Posiva Oy. POSIVA Report 2010-01. 478 p.
- Posiva (2009). Olkiluoto Site Description 2008, POSIVA report 2009-01.
- Posiva (2012). Olkiluoto Site Description 2011, POSIVA report 2011-2.
- Posiva (2013a). Backfill design 2012. POSIVA Report 2012-15.
- Posiva (2013b) Backfill production line. POSIVA Report 2012-18.
- Schatz, T. & Martikainen, J. (2012). Laboratory tests and analyses on potential Olkiluoto backfill materials. Posiva Oy, Eurajoki, Finland. Working Report 2012-74.

APPENDIX A. ANALYTICAL SOLUTION FOR GAP INTRINSIC PERMEABILITY (Mattias Åkesson, Clay Technology AB)

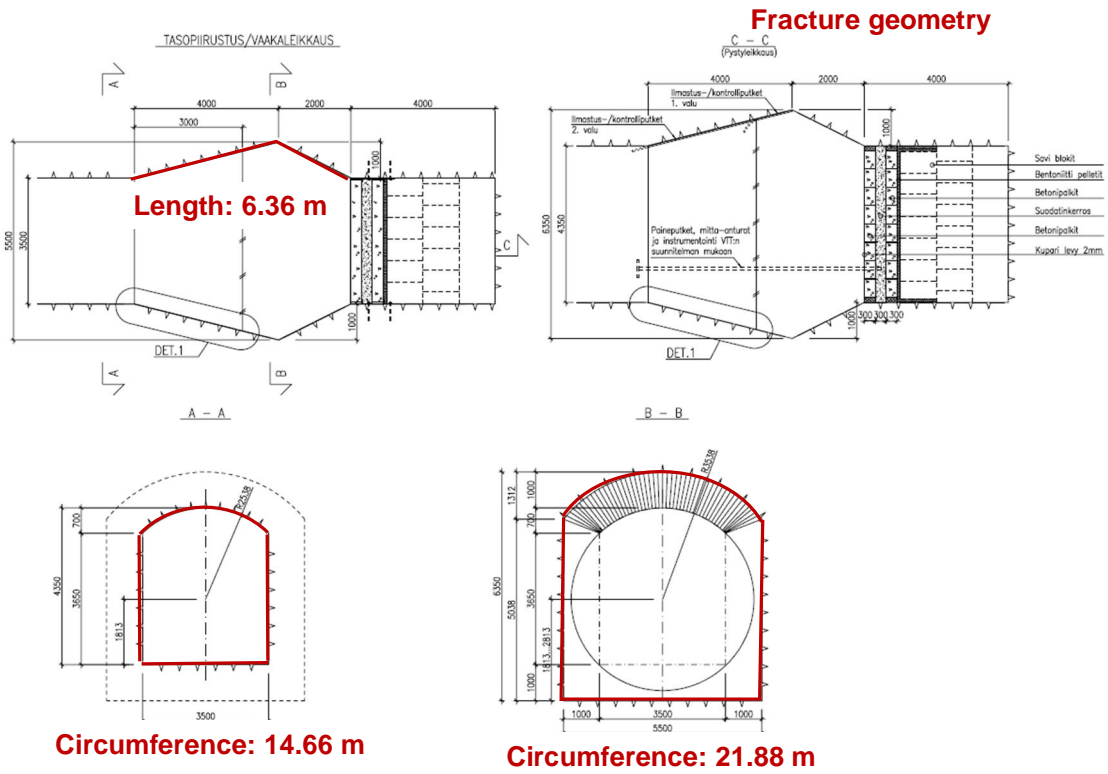
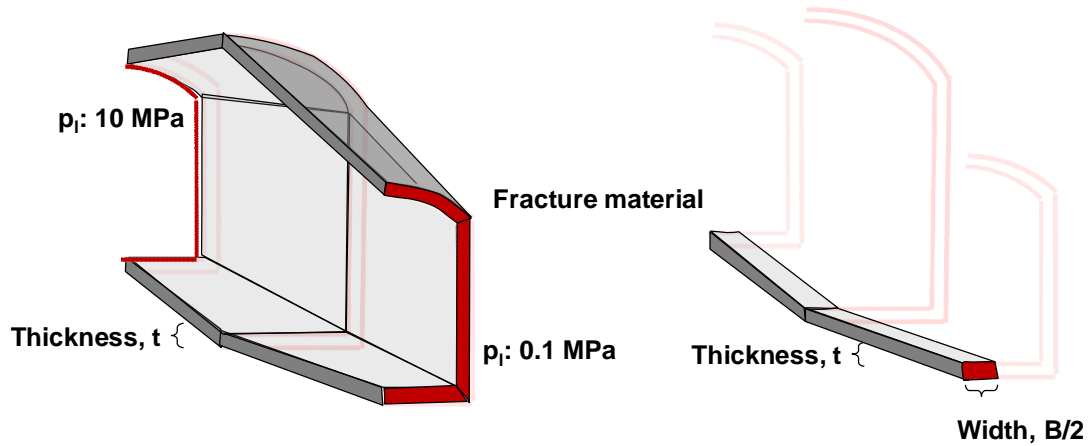


Figure A-1. Geometry used in the analytical solution.

Parameters and constants:			
Specific weight of water:	$\rho g = 9810$	(Pa/m)	
Water viscosity:	$\mu = 10^{-3}$	(Pa*s)	
Litres/m ³ & sec/min:	$l_{pm} = 10^3 \cdot 60$		
Geometry:			
Length of plug:	$L_p = 6.4$	(m)	$\sqrt{4^2 + 1^2} + \sqrt{2^2 + 1^2} = 6.36$
Mean circumference:	$O_p = 18$	(m)	$(14.66 + 21.88) \cdot \frac{1}{2} = 18.27$
Hydraulic relations:			
Flow rate:	$Q_p = \frac{0.1}{l_{pm}}$		
Head (9.9 MPa):	$h_H = \frac{9.9 \cdot 10^6}{\rho g}$	$h_H = 1009.17$	(m)
Gap transmissivity:	$T_f(B) = \frac{Q_p \cdot L_p}{B \cdot h_H}$	Gap width: 18 m	Gap width: 0.1 m
		$T_f(18) = 5.87 \times 10^{-10}$	$T_f(0.1) = 1.06 \times 10^{-7}$ (m ² /s)
Thickness of gap material:	$\Delta x = 0.1$	(m)	
Hydraulic conductivity of gap material:	$K_f(B) = \frac{T_f(B)}{\Delta x}$	Gap width: 18 m	Gap width: 0.1 m
		$K_f(18) = 5.87 \times 10^{-9}$	$K_f(0.1) = 1.06 \times 10^{-6}$ (m/s)
Intrinsic permeability of gap material:	$k_f(B) = \frac{\mu}{\rho g} \cdot K_f(B)$	Gap width: 18 m	Gap width: 0.1 m
		$k_f(18) = 5.99 \times 10^{-16}$	$k_f(0.1) = 1.08 \times 10^{-13}$ (m ²)

Figure A-2. Analytical solution and intrinsic permeabilities.



$K = T/t$
 K: Hydraulic conductivity (m/s)
 T: Transmissivity (m²/s)
 t: thickness (m), = e.g. 0.1 m

Figure A-3. Boundary conditions (MPa) in case A (left) and cases B and C (right).

APPENDIX B. BENTONITE INTRUSION INTO POPLU SLOT (Mattias Åkesson, Clay Technology AB)

The "POPLU seal" is planned to be made of swelling clay, e.g. of *in situ* compacted granular bentonite, that is installed inside a perforated frame. Once the water in the "pressurised POPLU section" penetrates through the perforated frame to saturate the swelling clay, the clay is intended to penetrate into the possible gap between the concrete plug and the host rock. This way the "POPLU seal" is assumed to make the plug watertight.

One approach for describing this process is presented in this appendix. All properties and conditions used are the same as in a similar study presented in SKB TR-09-34, and these may be revised later on.

The stress distribution $\sigma(z)$ in the intruded bentonite is given by the boundary stress (σ_0), the aperture of the slot, the friction angle (φ) and the following relation (Figure B-1, left):

$$s(z) = s_0 \exp\left(-\frac{2z}{d} \tan \varphi\right) \quad (\text{B1})$$

The length of the intruded bentonite is defined as the distance at which the stress level is 10 Pa:

$$L_B = \ln\left(\frac{s_0}{10 \text{ Pa}}\right) \frac{d}{2 \tan \varphi} \quad (\text{B2})$$

The boundary stress (σ_0) is set to 7000 kPa in the calculations below.

The swelling pressure and the hydraulic conductivity of MX-80 are described by void ratio dependent relations: $p_{sw}(e)$ and $K(e)$, respectively, see Figure B-1, right. These relations are interpolated from tables presented in SKB TR-09-34.

A void ratio distribution can thus be evaluated from the inverse function of the swelling pressure relation (Figure B-2, left):

$$e(z) = p_{sw}^{-1}(s(z)) \quad (\text{B3})$$

This, in turn, can be used to evaluate a distribution of the hydraulic conductivity: $K(z)$, Figure B-2, right.

The transmissivity for a slot with intruded bentonite can be derived in the following way. The water flux through the bentonite (q_B) is constant:

$$q_B = K(z) \frac{dh}{dz} = \text{const.} \quad (\text{B4})$$

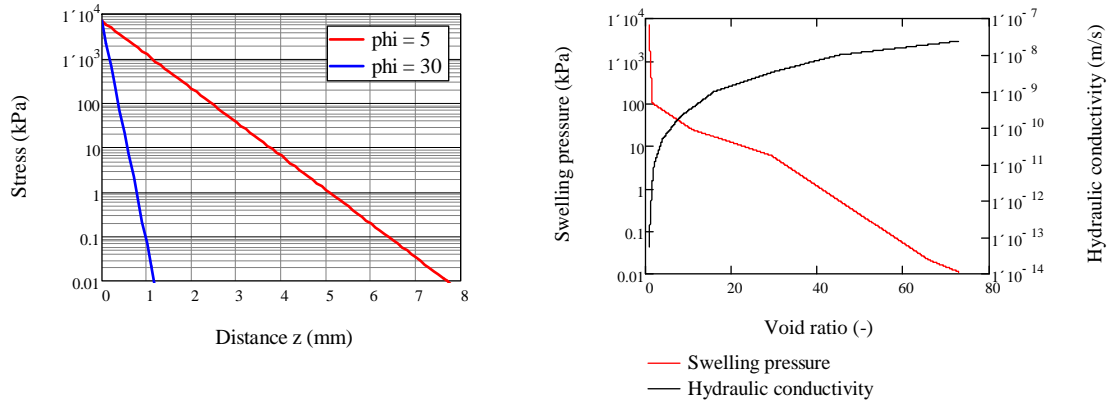


Figure B-1. Stress distribution in intruded bentonite for different friction angles and an aperture of $100 \mu\text{m}$ (left); void ratio dependent relations for swelling pressure and hydraulic conductivity (from TR-09-34, right).

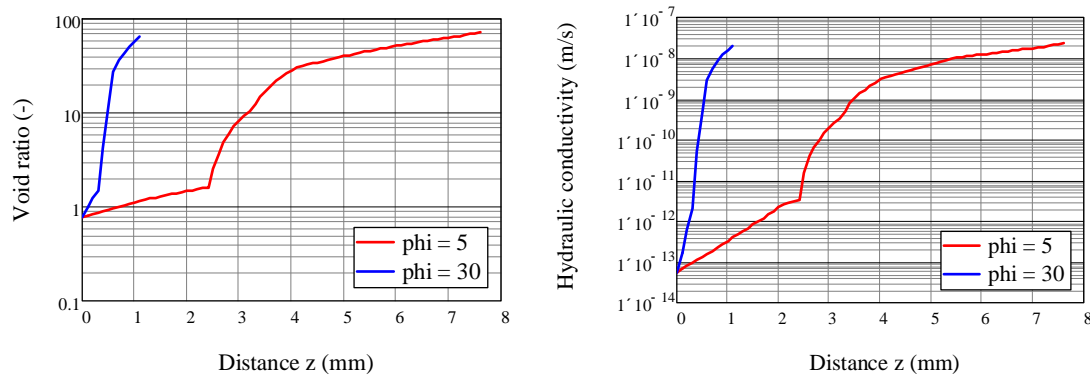


Figure B-2. Void ratio (left) and hydraulic conductivity (right) distribution in intruded bentonite for different friction angles and an aperture of $100 \mu\text{m}$.

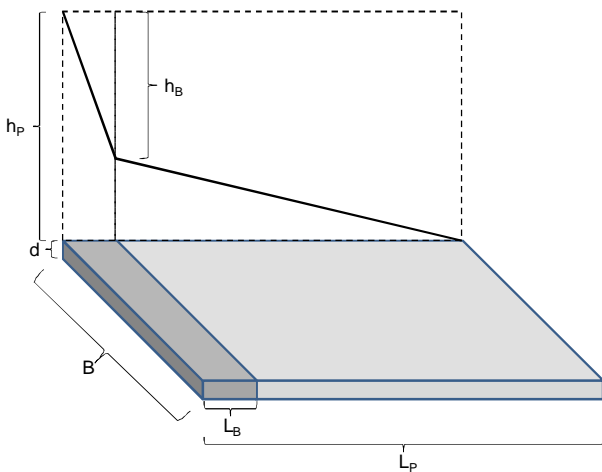


Figure B-3. Schematic illustration of slot with intruded bentonite.

The derivative dh/dz is the hydraulic gradient. The total head difference of the intruded bentonite (h_B) is equal to the integral of the hydraulic gradient, which in turn is equal to the integral of the ratio between the flux and the hydraulic conductivity:

$$h_B = \int_0^{L_B} \frac{dh}{dz} dz = \int_0^{L_B} \frac{q_B}{K(z)} dz \quad (\text{B5})$$

This can be re-arranged to:

$$q_B = \frac{h_B}{\int_0^{L_B} \frac{dz}{K(z)}} \quad (\text{B6})$$

The flow rate (Q_B) is given by the product of the flux and the section area ($B \cdot d$), and can also be expressed in terms of the transmissivity T_B :

$$Q_B = B \times d \times q_B = \frac{B \times d \times h_B}{\int_0^{L_B} \frac{dz}{K(z)}} = B \times T_B \times \frac{h_B}{L_B} \quad (\text{B7})$$

This can be re-arranged to:

$$T_B = \frac{d \times L_B}{\int_0^{L_B} \frac{dz}{K(z)}} \quad (\text{B8})$$

This quantity appears to be independent of the friction angle and is calculated to $7.6 \cdot 10^{-17} \text{ m}^2/\text{s}$ for a case with a boundary stress of 7000 kPa and an aperture of 100 μm , see also Figure B-4, left.

The transmissivity of the slot without any intruded bentonite is given by:

$$T_f = \frac{r g d^3}{m 12} \quad (\text{B9})$$

In order to quantify the sealing effect, the ratio between the flow rate for cases with and without intruded bentonite is calculated. For a case with no bentonite the flow rate is:

$$Q_P^{nb} = B \times T_f \times \frac{h_P}{L_P} \quad (\text{B10})$$

For a case with bentonite the flow rate is:

$$Q_P^b = B \times T_f \times \frac{h_P - h_B}{L_P - L_B} = B \times T_B \times \frac{h_B}{L_B} \quad (\text{B11})$$

After some operations this can be expressed as:

$$Q_P^b = \frac{B > h_P}{\frac{L_P - L_B}{T_f} + \frac{L_B}{T_B}} \tag{B12}$$

The ratio between the two cases can be expressed as:

$$\frac{Q_P^b}{Q_P^{nb}} = \frac{\frac{B > h_P}{\frac{L_P - L_B}{T_f} + \frac{L_B}{T_B}}}{B \times T_f \times \frac{h_P}{L_P}} = \frac{1}{\frac{L_B}{L_P} \frac{T_f}{T_B} - 1} + 1 \gg \frac{L_P}{L_B} \frac{T_B}{T_f} \tag{B13}$$

This ratio is illustrated as a function of the aperture in Figure B-4, center. For aperture values higher than 10 μm the flow rate appears to be reduced with at least four orders of magnitude.

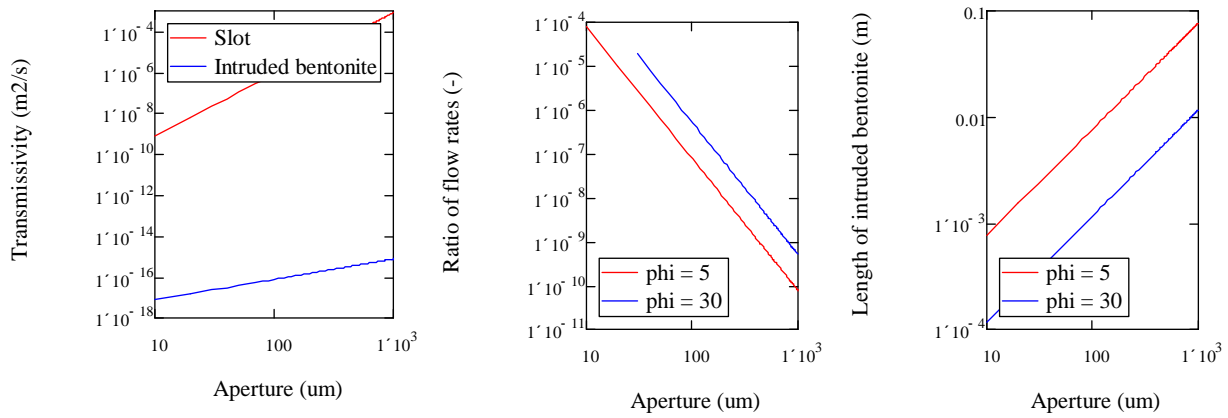


Figure B-4. Transmissivity as a function of aperture for cases with and without intruded bentonite (left). Ratio between flow rate for cases with and without intruded bentonite as a function of aperture (center). Length of intruded bentonite as a function of aperture (right).